RESEARCH ARTICLE

Scales of seafloor sediment resuspension in the northern Gulf of Mexico

Arne-R. Diercks[*], Clayton Dike[*], Vernon L. Asper[*], Steven F. DiMarco[†], Jeffrey P. Chanton[‡] and Uta Passow[§]

Seafloor sediment resuspension events of different scales and magnitudes and the resulting deep (>1,000 m) benthic nepheloid layers were investigated in the northern Gulf of Mexico during Fall 2012 to Summer 2013. Time-series data of size-specific *in-situ* settling speeds of marine snow in the benthic nepheloid layer (moored flux cameras), particle size distributions (profiling camera), currents (various current meters) and stacked time-series flux data (sediment traps) were combined to recognize resuspension events ranging from small-scale local, to small-scale far-field to hurricane-scale. One small-scale local resuspension event caused by inertial currents was identified based on local high current speeds (>10 cm s^{-1}) and trap data. Low POC content combined with high lithogenic silica flux at 30 m above bottom (mab) compared to the flux at 120 mab, suggested local resuspension reaching 30 mab, but not 120 mab. Another similar event was detected by the changes in particle size distribution and settling speeds of particles in the benthic nepheloid layer. Flux data indicated two other small-scale events, which occurred at some distance, rather than locally. Inertia-driven resuspension of material in shallower areas surrounding the traps presumably transported this material downslope leaving a resuspension signal at 120 mab, but not at 30 mab. The passage of hurricane Isaac left a larger scale resuspension event that lasted a few days and was recorded in both traps. Although hurricanes cause large-scale events readily observable in sediment trap samples, resuspension events small in temporal and spatial scale are not easily recognizable in trapped material as they tend to provide less material and become part of the background signal in the long-term averaged trap samples. We suggest that these small-scale resuspension events, mostly unnoticed in conventional time-series sampling, play an important role in the redistribution and ultimate fate of sediment distribution on the seafloor.

Introduction

The sedimentation of large amounts of oil via marine snow and its accumulation on the deep seafloor (>1,200 m) during and after the Deepwater Horizon (DwH) oil spill (Passow et al., 2012; Valentine et al., 2014; Brooks et al., 2015; Chanton et al., 2015; Daly et al., 2016; Joye, 2016; Joye et al., 2016; Passow, 2016) raised questions regarding the distribution and re-distribution processes of freshly sedimented material (marine snow) on the seafloor. Once on the seafloor, marine snow contributes to unconsolidated fluffy sediment layers (Gardner, 1978; Gardner et al., 1984; 1985; Walsh et al., 1988; Pilskaln et al., 1998; Newell et al., 2005) that are subject to resuspension and the production of benthic nepheloid layers (BNLs).

Resuspension leads to the re-invigoration of degradation processes, which would impact the degradation rates of the oil associated with marine snow following the DwH accident (Ziervogel et al., 2016). Additionally, resuspension leads to lateral transport and redistribution of the material that sank to the seafloor. After the DwH accident such re-distribution processes make it especially difficult to estimate the total amount of *Macondo* oil that reached the seafloor (Passow and Hetland, 2016).

BNLs, which are formed when the frictional stress of water motion strips sediment off the seafloor, therewith carrying particles into the overlying water layer, exist near the seafloor, but may reach tens to hundreds of meters upward into the water column (McCave et al., 1976). The thickness of the BNL extending above the seafloor scales with the strength of the bottom currents and the particle composition. Bottom currents >10 cm s^{-1} may cause resuspension events (Gardner et al., 2017), especially when low density phytodetritus or fine silt covers sediments, but large benthic storms reach 20 cm s^{-1} (Gardner et al., 1985). Besides locally resuspended material, particles in the BNL also include aggregates settling from the upper ocean as

[*] University of Southern Mississippi, Stennis Space Center, Mississippi, US

[†] Texas A&M University, College Station, Texas, US

[‡] Florida State University, Tallahassee, Florida, US

[§] University of California at Santa Barbara, Santa Barbara, California, US

Corresponding author: Arne-R. Diercks (arne.diercks@usm.edu)

well as laterally advected particles, possibly resuspended further afield or earlier. When not replenished with new particles, these turbidity layers have a lifetime of days, allowing for appreciable lateral advection. The fraction of resuspended particles versus those settling from the surface ocean may be estimated from the clear water minimum of a whole water profile.

Lateral transport of BNLs can reach especially far, if resuspension events occur at shallower depth compared to the surrounding regions, e.g., on a sea mount, or on a shelf near the shelf break. Material originally sedimented in such shallower areas may easily be transported to deeper regions where flux stemming from the surface ocean may be relatively small. Total flux in such regions may thus exceed local production significantly. In the Gulf of Mexico, exchange processes between the continental shelf, the slope, and the deep basin are poorly constrained and include eddy-topography interactions (Sutyrin et al., 2003), river plumes, buoyancy-driven circulation, wind-driven canyon flow (Yuan, 2002), episodic storm-induced resuspension events (Walsh et al., 1988; Ziervogel et al., 2016), and upwelling. Due to such exchange, material originating from shallow areas may enter the deep ocean.

Here we explored resuspension events of different spatial and temporal scales and magnitudes and the resulting BNLs in the northern Gulf of Mexico during Fall 2012 to Summer 2013. Our investigation focused on a station about 1,500 m deep near the DwH spill site, OC26, where the effects of several small resuspension events, driven by inertial currents lasting only hours, were observed. Two of these inertial resuspension events that left a flux signature at OC26 were local, and two occurred farther away

(far-field) with material advected into the investigation area. A large-scale resuspension event, associated with the passage of Hurricane Isaac, also left a resuspension signature at OC26 during the period of study. These events left visible signatures in: (i) vertical flux difference between stacked traps at 30 m above bottom (mab) and 120 mab, (ii) marine snow size and settling speed measured at 80 mab, (iii) current speeds and direction near the seafloor, and (iv) marine snow profiles showing BNLs. For comparison, some data from a second site, GC600, which is further offshore and above a natural seep field, are presented.

Methods

To investigate resuspension and the formation of BNLs in the northern Gulf of Mexico, we combined data from flux cameras, a profiling camera, various current meters and time-series sediment traps. The emphasis of our work is on a station about 3.8 km south of the DwH *Macondo* wellhead (OC26: 28° 40.776' N; 88° 21.648' W), located in the Mississippi Canyon lease block 297 (**Figure 1**). OC26 is located downslope off the continental shelf between several diapiric salt domes, *Gloria Dome* to the east, *Biloxi Dome* to the west, and *Mitchell Dome* to the northeast (**Figure 2**). These domes, which surround OC26, rise between 200 to 500 m above the seafloor. Seafloor depths near OC26 range from 1,170 m on top of the salt domes to a maximum depth at the sediment trap location of 1,641 m. For a detailed description of the bathy-morphology see Conti et al. (2016). The main mooring at this site was equipped with two sediment traps, an ADCP and a flux camera. Additionally, single-point current meters were deployed in the vicinity (**Figure 1**).
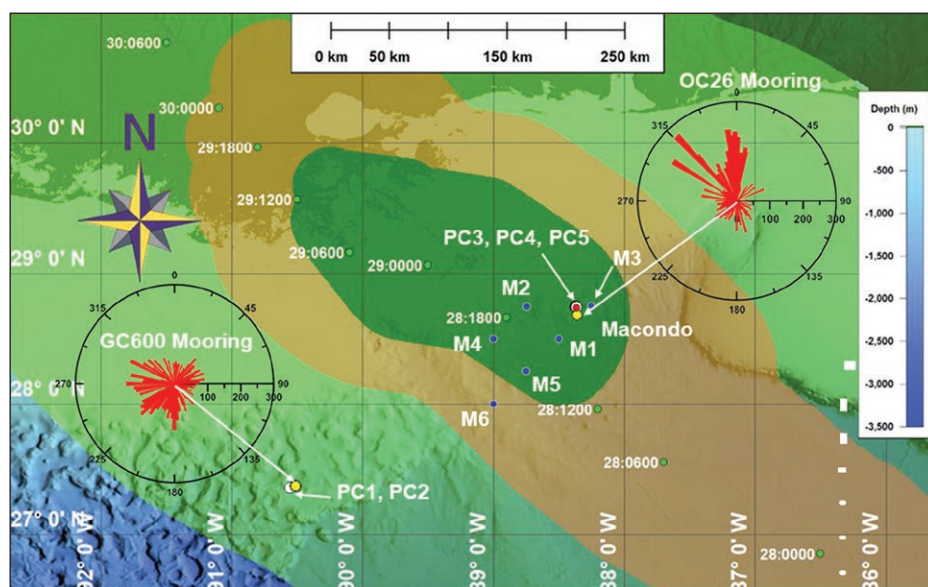

Figure 1: Overview map of site locations. White dots indicate locations of profiling camera casts PC1 to PC5. Yellow dots indicate locations of sediment trap moorings. Red dot indicates the location of the *Macondo* wellhead. Dark green area indicates Hurricane Isaac wind swath with wind speeds >64 mph; brown, wind speeds >49.33 mph; and light green, wind speeds of >39 mph. Locations of the center of the hurricane eye are plotted as green dots with day and time in August of 2012 (e.g. 28 0600 indicates 28 August 2012 at 6:00 am). Blue dots mark the M1 to M6 mooring locations where the Gulf Integrated Spill Research (GISR) consortium deployed single-point current meters. Polar diagrams depict ADCP current measurements from the sediment trap moorings from 25 August 2012 to 5 September 2012, the passage of Hurricane Isaac. Currents are plotted with the indicator point from the center in the direction of the flow. DOI: https://doi.org/10.1525/elementa.285.f1
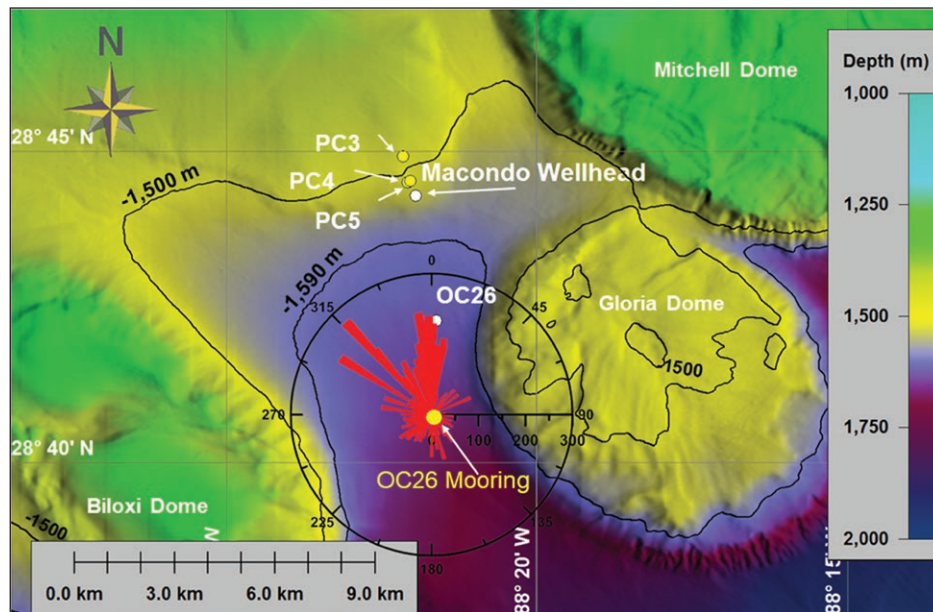
Figure 2: Site locations for profiling camera casts PC3 to PC5 and the trap mooring near OC26. Polar diagram depicts the currents at depth of flux camera during the period of 28 August to 4 September 2012 recorded by the ADCP on the trap mooring at OC26. Current directions are pointing from the center outward, with two main directions, one to the northwest and one north. Note the location of the trap mooring in the valley between the *Biloxi* and *Gloria* domes and that the main current directions are aligned with the seafloor morphology at the trap mooring site. Color scale bar indicates depth below sea surface (m). DOI: https://doi.org/10.1525/elementa.285.f2

The comparison site, GC600 (27° 22.529' N, 90° 30.828' W), is located within the Green Canyon lease block 600, about 185 km to the southwest of the DwH site at a depth of ~1,200 m. GC600 is an area of active natural hydrocarbon seepage (Garcia-Pineda et al., 2014), and a flux camera and one sediment trap were deployed approximately 5.4 km to the east of the main known hydrocarbon seepage (Roberts et al., 2010; Joye, 2016).

Cameras
Profiling camera
A profiling camera modified from the original design of Honjo et al. (1984) and Asper (1987) was used to assess vertical distribution of marine snow. A total of five profiling camera casts (PC1 to PC5), each profiling from the surface to the seafloor, were performed during the Fall 2012 Endeavor cruise EN515 (**Table 1**): two daily casts, PC1 and PC2, were taken at GC600 on 7–8 September 2012, and three daily casts, PC3 to PC5, were conducted 12–14 September 2012 near OC26. A simplified version of PC3 to PC5 was presented by Ziervogel et al. (2016) as marine snow camera (MSC) profiles 3, 4 and 5, but size distribution was mislabeled (see erratum). General characteristics of other casts, sampled between 2015 and 2017, are not discussed in detail, but are listed in **Table 1** as a measure of the prevalence of benthic nepheloid layers in this region.

A Seabird SeaCat-19 CTD provided the depth for each recorded image. The clocks in the CTD and the camera were synchronized before each cast. Camera metadata of frame number, time, and exposure settings were recorded with each image and matched to the corresponding CTD time to determine the depth of each image. The camera was programmed to take an image every 11 seconds, and the camera frame was lowered through the water column at 10 m min⁻¹ capturing an image at a vertical depth interval of 1.8 m.

All images were processed using Image-Pro® Plus software. A calibration image with an object of known size was taken during the cruise, by placing a reference object of known size within the cameras focal point. Based on the illuminated area in the images of each cast, an area of interest was selected for a specific cast, the dimensions measured and a volume of illuminated water calculated. All particles larger than 0.5 mm in diameter, the lower size limit for marine snow, were counted and sized by the software. Any identifiable objects that were not marine snow, e.g., bubbles, zooplankton, fish, etc., were marked and removed before the counting of particles in each image. Counted particles were volume-normalized and binned by size. During post-processing, particles were binned in 10-m vertically averaged size bins. Image depths were determined by correlating the times recorded within the synchronized CTD data of the same cast with the time stamps recorded within the exchangeable image file data stored with each image.

Flux camera
To determine the settling speed of marine snow near the seafloor, flux cameras, described in Diercks and Asper (1997), were deployed 80 mab at OC26 and GC600 together with the traps. Size and settling speeds of settling particles were recorded at hourly or bi-hourly intervals for several months in 2012 and early 2013 (**Table 2**). At GC600 a total of 2335 particles, or 9 ± 5 particles every 2 hours, were analyzed for size and settling speed. Size and settling speed analysis at OC26 were based on 907

Table 1: General characteristics of profiling camera (PC) casts. DOI: https://doi.org/10.1525/elementa.285.t1

Cast[a]	Latitude (N)	Longitude (W)	Date	Site	Max camera depth (m)	Water depth (m)	BNL	Volume analyzed (L)
PC1	27° 21.320′	90° 33.370′	7 Sep 2012	GC600	1,274	1,287	No	3.43
PC2	27° 22.417′	90° 30.693′	8 Sep 2012	GC600	1,369	1,384	Yes	3.25
PC3	28° 44.915′	88° 22.151′	12 Sep 2012	OC26	1,473	1,483	Yes	3.16
PC4	28° 44.503′	88° 22.072′	13 Sep 2012	OC26	1,463	1,506	Yes	2.91
PC5	28° 44.521′	88° 22.038′	14 Sep 2012	OC26	1,472	1,506	Yes	3.16
1	27° 22.292′	90° 34.287′	27 Apr 2016	GC600	1,185	1,203	Yes	9.95
2	27° 24.180′	91° 49.970′	29 Apr 2016	GC574	1,030	1,053	Yes	9.95
3	27° 07.400′	91° 23.840′	29 Apr 2016	GC847	1,755	1,765	Yes	9.95
4	27° 06.800′	91° 21.050′	29 Apr 2016	GC847	1,745	1,765	Yes	9.95
5	27° 12.660′	91° 00.140′	30 Apr 2016	GC767	1,574	1,600	Yes	9.95
6	27° 12.560′	91° 00.180′	1 May 2016	GC767	1,580	1,600	Yes	9.95
7	27° 21.991′	90° 34.229′	2 May 2016	GC600	1,148	1,200	Yes	9.95
8	27° 21.214′	91° 49.284′	8 Aug 2016	GC574	1,045	1,053	Yes	9.95
9	27° 21.160′	91° 49.240′	8 Aug 2016	GC574	1,047	1,053	Yes	9.95
10	27° 00.287′	91° 17.560′	11 Aug 2016	EN586-17	2,370	2,383	Yes	9.95
11	27° 17.522′	90° 02.435′	13 Aug 2016	GC699	1,328	1,365	Yes	9.95
12	27° 31.646′	89° 42.402′	11 Jun 2017	GC185	517	527	Yes	9.95
13	27° 22.342′	90° 34.295′	12 Jun 2017	GC600	1,185	1,203	Yes	9.95
14	27° 17.522′	89° 59.029′	17 Jun 2017	GC699	1,313	1,320	Yes	9.95
15	27° 21.170′	91° 49.280′	19 Jun 2017	GC574	1,043	1,053	No	9.95
16	27° 46.986′	91° 30.413′	24 Jun 2017	GC185	530	540	Yes	9.95
17	27° 21.816′	90° 33.706′	26 Jun 2017	GC600	1,212	1,220	Yes	9.95
18	28° 40.695′	88° 21.420′	27 Jun 2017	OC26	1,614	1,624	Yes	9.95

[a] Camera casts listed as 1 to 18 are for reference of BNL presence only; specific data from these casts are not discussed further.

Table 2: Flux camera deployments and imaging intervals. DOI: https://doi.org/10.1525/elementa.285.t2

Site	Deployment period	Data collection period	Intervalometer settings (s)
OC26	26 June–9 Sept 2012	26 June–9 Sept 2012	60 | 60 | 120 | 240 | 3120
OC26	11 Sept 2012–18 Oct 2013	11 Sept 2012–17 Feb 2013	60 | 60 | 60 | 60 | 120 | 240 | 480 | 6120
GC600	8 Sept 2012–5 June 2013	8 Sept–27 Dec 2012	60 | 60 | 120 | 120 | 240 | 3000

and 1,910 individual particles, equivalent to 8 ± 6 and 4 ± 2 particles every 2 hours, respectively, during periods 1 and 2. Each camera system, built by Ocean Imaging Systems, included a single Nikon D7000 DSLR camera equipped with an external intervalometer, enclosed in a HBR-1600 pressure housing rated to 6,000 m. Each flux camera was mounted in a 0.61 m × 0.91 m open frame cage, oriented to take pictures of a 0.203 m × 0.203 m clear acrylic settling chamber. The settling chamber was sealed on the sides to prevent seawater exchange. A 1.22-m long PVC stilling chimney (0.102 m in diameter) was attached to the top of the settling chamber allowing particles to enter. A strobe, mounted orthogonally to each camera/viewing chamber line, illuminated particles within the settling chamber. The Nikon D7000s were set to record images at f/22, 1/60s, using ISO-100.

Images were taken in bursts every hour or every other hour followed by a shutdown of the system to conserve battery and memory. The installed intervalometers triggered the camera at preset intervals (**Table 2**) that were programmed to allow an individual particle to be imaged multiple times as it settled in the settling chamber. After the first recovery of the camera at OC26, many particles were observed to have settled faster than the intervals could resolve. Slow settling particles were tracked across several images, but the average settling speed estimates are assumed to be too low, because rapidly settling particles were missed. A minimum settling speed of 185 m d^{-1}, based on the camera

setup, was assigned to particles that were only encountered in a single image. The intervalometer was reprogrammed for the second deployment using four 60-second intervals to resolve more fast-settling particles. Efficiency of capturing settling particles on more than a single image during the flux camera deployments was between 2% and 68%, suggesting that a large number of particles settled at much higher settling speeds and that the settling speeds reported here are biased to the slower ones. The GC600 camera system suffered a strobe failure in late December 2012, during the first deployment, which limited the number of images collected during the first deployment and prevented the redeployment of the system.

Images were processed using Image-Pro® Plus software. A calibration file was created for each deployment, and the individual images were processed in sequenced bursts. Area, perimeter, diameter (mean), settling speed, number of aggregates, and image time were recorded. A tracking program for marine snow aggregates was developed and used to determine settling speeds of all settling marine snow aggregates with a mean diameter >0.5 mm found in at least two consecutive images. Marine snow aggregates were tracked only if their measurements on subsequent images fell within all the following gates applied to parameters of precedent or subsequent particles: area ± 0.25 mm², center-Y ± 10 mm, angle ± 90°, diameter ± 0.5 mm, and roundness ± 1. Area was the cross-sectional area of the particle, center-Y was the Y coordinate of the image that gives the horizontal position of the particle in the viewing chamber, angle was the angle of orientation of the particle, diameter was the mean diameter of the particle, and roundness was the perimeter divided by 4π and the area of the marine snow aggregate.

Flux calculation

Velocity (v_s) of a terminally settling particle is found by solving Equation 1. Given that we have measured individual size specific settling speed, Stokes' equation can be rearranged and solved for the particle density. As commonly known, Stokes' law describes perfect spheres of uniform density. Marine snow particles are rarely spherical nor uniform in density or material. Deviations from a spherical shape may reduce or increase drag based on the shape of the aggregate, similarly as density and porosity. Passow et al. (2012) presented that 99.7% of the volume of marine snow from the Gulf of Mexico was water, highlighting the equation of dry weight being a function of particle volume and porosity (Equation 2).

Stokes' law and settling speed to calculate particle density:

$$v_s = \frac{2}{9}\frac{\left(\rho_p - \rho_f\right)}{\mu}g\,R^2 \qquad \text{(Eq. 1)}$$

$$DW = \rho_P V\left(1-P\right)\left(1\right) \qquad \text{(Eq. 2)}$$

where ρ_p is the particle density, ρ_f is the fluid density, μ is dynamic viscosity, g is gravitational acceleration, R is the particle radius, DW is dry weight, V is the particle volume, and P is particle porosity.

To overcome some of the pitfalls of using Stokes' equation to determine marine snow settling speeds, Ploug et al. (2010) incorporated the Reynolds number (Re; Equation 3) in their drag coefficient (C_d; Equation 4) to develop their modified Stokes equation (Equation 5). Introducing the coefficient of Drag (C_d) into the Stokes settling equation Ploug et al. (2010) derived a modified Stokes' equation (Equation 5):

$$Re = \frac{\rho_f v_s D}{\mu} \qquad \text{(Eq. 3)}$$

$$C_d = \frac{24}{Re} \qquad \text{(Eq. 4)}$$

$$v_s = \sqrt{\frac{4}{3}*\left(\rho_P - \rho_f\right)*\frac{gD}{\rho_f C_d}} \qquad \text{(Eq. 5)}$$

Settling velocity based on Ploug et al. (2010) using particle excess density can be calculated as:

$$v_s = \left(\frac{2g\Delta\rho V}{\rho_f C_D A}\right)^{0.5} \qquad \text{(Eq. 6)}$$

where d is particle diameter, $\Delta\rho$ is aggregate excess density, and A is aggregate cross-sectional area. Particle densities were calculated for all particles with measured settling speeds based on Stokes' Law (Equation 1), modified Stokes' Law (Equation 5), Ploug et al. (2010; Equation 6) and the Maggi (2013) equation for modeling settling speeds using fractal dimensions (see below). Results of all four calculations varied in the 5th decimal behind the comma for weight.

Maggi (2013) used fractal theory to more realistically describe individual particle shapes and dimensions and tested his model against published size-specific settling speeds of aggregates. For our density calculations we used his T-51 test values for *in-situ* marine snow aggregates collected by Shanks and Trent (1980). Using his (Maggi, 2013) fractal model (Equation 7), and substituting the individual shape factors H, K and Z^2 with Equations 8, 9 and 10, the particle density can be derived in Equation 11:

$$V_s = \frac{-18\mu H \pm \sqrt{18^2\mu^2 H^2 + 6gD^3\rho_f\left(\rho_p - \rho_f\right)Z^2}}{3D\rho_f K} \qquad \text{(Eq. 7)}$$

$$H = \frac{3}{9}\sqrt{\pi}\left(D^2\pi / 4\right)^{\left[\alpha / \left[\sigma^2 l^2\gamma\right]+\beta\right] / 2} \qquad \text{(Eq. 8)}$$

$$K = \frac{\pi}{6}D \qquad \text{(Eq. 9)}$$

$$Z^2 = \frac{\pi^2}{36}D^2 l^{\delta l\gamma-3} \qquad \text{(Eq. 10)}$$

where l = L / L$_p$ (diameter of the aggregate divided by the diameter of the primary particles), α = 9/8 and β = 7/8

(derived by Maggi and Winterwerp, 2004), $L_p = 0.78$ μm, $\rho_p = 1300$ kg m^{-3}, $\delta = 2.86$, and $\gamma = -0.0430$ from Maggi's T51-Test (Maggi, 2013) based on data published by Shanks and Trent (1980). We can rearrange his settling speed equation to solve for particle density, using our measured settling speeds and sizes. Density of the settling particle ρ_s can thus be calculated as:

$$\rho_s = \frac{\nu_s K \left(3\nu_s D\rho_f K + 36\mu H\right)}{2gD^2 z^2} + \rho_f \qquad \text{(Eq. 11)}$$

The intervalometer settings of the flux camera recorded images 5% of the time (360 seconds out of every 7,200 seconds) during deployment 1 and 15% (1,080 seconds out of every 7,200 seconds) during deployment 2. After normalizing the data collection time of the camera system to that of the sediment trap, a particle mass flux (mg m^{-2} d^{-1}) was calculated by using the suggested porosity of 99.7% for Gulf of Mexico marine snow particles (Passow et al., 2012). For the available flux camera data, the integrals of mass flux over each 18-day period corresponding to the lower trap schedule were calculated. A correlation between the calculated dry weight flux of the flux camera and the lower sediment trap ($r^2 = 0.85$, n = 13) was found; however, the calculated camera flux was 2.5 times larger than that of the lower sediment trap. This difference could be due to the unlikely effect of the flux camera collecting systematically different material from the trap or, more likely, to the assumptions for parameters, e.g., shape and porosity, in the calculations of the mass flux derived from size-specific aggregate settling speeds causing an overestimation of the actual flux.

Sediment traps

Two 21-cup PARFLUX sediment traps, described in detail in Honjo et al. (1982), were deployed at OC26 between June 2012 and October 2013 at 30 mab and 120 mab (**Table 3**). A third sediment trap was deployed at GC600 at 120 mab. Here we present mass flux (DW), flux of lithogenic silica (LSi) and the ratio between particulate organic carbon and mass flux (POC:DW), as well as the mineral content and the δ^{34}S ratio of settling material. Data from the traps at 120 mab at GC600 and OC26 are presented in more detail elsewhere (Giering et al., 2018).

Flux of LSi was calculated as:

$$LSi = DW - \left(CaCO_3 + bSiO_2 + 2.2\ POC\right) \qquad \text{(Eq. 12)}$$

where DW = dry mass, $CaCO_3$ = calcium carbonate flux, $bSiO_2$ = biogenic silica flux, and POC = particulate organic carbon flux. DW was determined in quadruplicate as the difference between dried and pre-weighed filters (450°C

for 4–6 hours; GF/F filters, 25-mm diameter, Whatman). DW flux was calculated as the total weight of the dried sample material collected on the filter devided by the collection area of the trap and the time of the cup being under the funnel, normalized to m^{-2} d^{-1}. After reweighing, the filters were used to determine POC and particulate inorganic carbon (PIC), each in duplicate. The POC filters were fumed with 10% HCl to remove inorganic carbon, and all filters were analyzed using a CHN elemental analyzer (CEC 44OHA; Control Equipment, now Exeter Analytical). PIC was defined as the difference of the acidified and non-acidified particulate carbon (Shipe and Brzezinski, 2003). Measured PIC+POC concentrations of cup 3 GC600 (16 October–3 November 2012) were unbelievably high and were corrected based on the PON values in the non-acidified versus acidified samples. Calcite ($CaCO_3$) content was calculated from PIC by assuming a molecular weight of 100. The $bSiO_2$ content was analyzed colorimetrically after hydrolyzation with Na_2CO_3 and running a 0.5- to 5-hour time series (Shipe and Brzezinski, 2001). The change in the slope of dissolution rate indicates the shift from $bSiO_2$ to lithogenic silica dissolution, and the intercept was used to determine $bSiO_2$ concentration. A molar mass of 67 was assumed for $bSiO_2$. For details on trap analysis, see Giering et al. (2018). Mineral content was calculated as the combined contributions of LSi, $CaCO_3$, and $bSiO_2$ to DW. Observed strong variations in total material flux are discussed in detail by Giering et al. (2018); however, similar high variations in total mass flux have been reported elsewhere. A more than hundred-fold increase in sediment trap mass flux between time-series samples was recorded by Roos and Valeur (2006) and was attributed to water column stratification.

Time periods where trap material indicated high likelihood of resuspension events were identified based on the POC:DW ratio of collected material and the relative sedimentation rates of LSi in the upper and lower traps. When resuspension of settled material and sediments is important, the POC:DW ratio in material collected with the traps should be low compared to time periods when sedimentation of particles from the surface ocean dominates trap collections. The flux of lithogenic material, which does not degrade or dissolve easily, should not decrease significantly during its 90-m descent between the two traps. Higher sedimentation rates in lower traps may thus indicate resuspension from below, whereas higher sedimentation in the upper trap would suggest lateral advection of mineral-rich material, e.g., stemming from distant resuspension events, e.g., on shelf slopes or from neighboring domes. Time periods were identified where POC:DW of settled material was ≤3.3% in either trap and where the smallest deviation from the one-to-one line of LSi flux in

Table 3: Sediment trap deployments. DOI: https://doi.org/10.1525/elementa.285.t3

Site	Latitude (N)	Longitude (W)	Deployment date	Recovery date	Water depth (m)
OC26	28° 40.780′	88° 21.680′	26 June 2012	09 Sept 2012	1,671
OC26	28° 40.780′	88° 21.680′	11 Sept 2012	18 Oct 2013	1,671
GC600	27° 22.466′	90° 30.689′	08 Sept 2012	30 Apr 2013	1,382

Table 4: Locations and depths of GISR[a] current meters. DOI: https://doi.org/10.1525/elementa.285.t4

Instrument	Latitude (N)	Longitude (W)	Water depth (m)	Height above bottom (m)	Deployment date (2012)	Recovery date (2013)
M1	28° 30.000'	88° 30.000'	1,690	13	6 July	8 July
M2	28° 44.900'	88° 44.780'	1,035	15	5 July	12 July
M3	28° 45.000'	88° 15.000'	1,337	20	6 July	8 July
M4	28° 30.000'	89° 00.000'	836	20	8 July	10 July
M5	28° 15.000'	88° 45.000'	1,650	20	8 July	10 July
M6	28° 00.000'	89° 00.000'	1,312	15	8 July	10 July
OC26	28° 40.780'	88° 21.680'	1,671	8	26 June	28 Oct

[a] Gulf Integrated Spill Research consortium results.

the upper and the lower trap was >95 mg m^2 d^{-1}, meaning LSi sedimentation rate was appreciably different between the two traps. A POC:DW ratio ≤3.3% was observed in less than one-fourth of the trap cups at OC26. These chosen boundary conditions are relatively arbitrary and meant to highlight a few cases where a possible resuspension signal was large enough to be visible in traps that collected material over a period of 17–18 days, and not meant to imply that no resuspension had occurred at other times. The identification of likely resuspension events based on trap data was not possible at GC600, as only one trap was moored at this station.

δ^{34}S values

Prior to sulfur isotope analysis, sample splits were freeze-dried, ground, soaked briefly with 10% HCl to remove minerals, rinsed with ultra-pure water and freeze-dried. Samples were then analyzed for stable sulfur isotopes (δ^{34}S) at the Stable Isotope Core Facility at Washington State University (Pullman, Washington). Analytical error measured as the coefficient of variation of replicate samples was 0.4‰ for δ^{34}S. In evaluating stable isotopes, the notation δ is used to indicate the ratio of two stable isotopes against the equivalent ratio in a known reference standard; δ^{34}S (‰) is defined as:

$$\delta^{34}S\ (‰) = \left[\left(R_{sample} - R_{standard}\right)/R_{standard}\right] * 1000 \quad \text{(Eq. 13)}$$

where R is the ratio of heavy (^{34}S) to light (^{32}S) isotope, referenced to the Canyon Diablo Troilite international standard value. Increases in δ^{34}S values denote increases in the relative amount of the heavy isotope ^{34}S; conversely, decreases in δ^{34}S values denote ^{34}S depletion relative to the standard material.

Current meters

Teledyne RDInstruments Workhorse Sentinel 300kHz ADCPs were deployed at OC26 and GC600, at about 8 mab and upward-looking, to record current data at the depth of the flux camera. The first sample bin was at 12 mab, with bin sizes of 4 m each, placing bin 7 from 40 to 44 mab. Frequently the ADCP signal was seen up to 80 mab. Binary current meter data were converted to ASCII for-

mat, using the WinADCP™ software provided by Teledyne RDInstruments, and values of magnitude and direction were extracted and averaged over a 25-hour sliding time bin. Six single-point current meters, deployed < 20 mab by the Gulf Integrated Spill Research (GISR) consortium in the region near the DwH site, collected current data from July 2012 to July 2013 (**Table 4**) (Spencer et al., 2016). Three of these moorings (M1–M3) surrounded the sediment trap at OC26: GISR mooring M1 was deployed 24 km to the SW of the OC26 mooring, M2 was deployed 38 km to the WNW of the OC26 mooring, and M3 was deployed 13 km to the ENE of the OC26 mooring on top of *Mitchell Dome* (**Figure 1**). Data from Fall 2012 are addressed in this paper.

Results

Profiling camera

Marine snow concentration at PC1 did not vary significantly in the upper 600 m of the water column, with a mean ± standard deviation of 6 ± 2 L^{-1} (n = 388, **Figure 3a**). From 600 to 1,200 m, the mean concentration of marine snow aggregates in all size classes increased to 18 ± 8 L^{-1} (n = 306). An approximately 50-m thick peak in particle concentration existed between 1,200 and 1,250 m (mean of 91 ± 30 L^{-1}, n = 30), below which concentrations decreased to a mean of 39 ± 26 L^{-1} (n = 18). The camera, lowered to within 13 m above the seafloor, recorded the top of a BNL with concentrations of 128 ± 12 L^{-1} at a depth of 1,273 m.

Marine snow abundance at PC2, taken near the sediment trap location at GC600, approximately 5.4 km east of PC1 (**Figure 3b**), was highly variable with depth, with no clear distinction between surface maximum, midwater minimum, and BNL. The highest concentrations of aggregates (mean 102 ± 41 L^{-1}, n = 152) were found in the upper 800 m of the water column, and the lowest (mean 42 ± 8 L^{-1}, n = 9) at the deepest part of the cast, 15 m above the seafloor. Volumetric percentage concentration of size distribution varied little over the entire water column, with an average of 10% of marine snow aggregates in the range of 0.5–1.0 mm, 46% in 1.0–1.5 mm, 36% in 1.5–2.0 mm, 6% in 2.0–2.5 mm, and the remaining 2% in the size fraction >2.5 mm (**Table 5**).

Casts PC3, PC4, and PC5 were taken within 48 hours in close vicinity of each other near the Macondo wellhead,

near OC26 (**Figure 2**) in mid-September 2012. All showed a clear BNL below about 1,200 m depth (**Figure 4**; **Table 5**). The upper boundary of the BNL was defined as the depth of the largest change in particle concentration. Whereas marine snow concentrations were low in all profiles, on average 11 ± 5 L^{-1} (n = 700) above the BNL, below 1,250 m, 1,230 m and 1,200 m marine snow concentrations increased abruptly to 75 ± 21 L^{-1} (n = 121), 124 ± 54 L^{-1} (n = 127), and 79 ± 46 L^{-1} (n = 118), in PC3, PC4 and PC5, respectively, positioning the upper boundary of the BNL at 233–306 mab. Peak concentrations of aggregates were found slightly lower, at 1,330 m (126 L^{-1}; PC3), 1,260 m (260 L^{-1}, PC4), and 1,247 m (211 L^{-1}, PC5), with decreasing marine snow concentrations below those depths. These profiles contrast especially with PC2, which was taken closer to GC600 where no BNL was evident (**Figure 3b**).

One day earlier, a clear BNL layer was, however, visible at GC600 as well (PC1; **Figure 3a**). The size fraction of marine snow < 1 mm (e.g., 0.5–1.0 mm) was low (4–22%) in all five profiles, with >75% of marine snow in the 1–2 mm size class. The size distribution in the BNL, specifically, was similar to that in the whole water column in profiles PC1 and PC5, but clearly different in PC3, and possibly in PC4, where marine snow >2 mm was more abundant (**Table 5**).

Comparison of the size frequency distribution of marine snow at OC26 between September 2012 and September 2014 (PC3–PC5) indicates rapid changes. Between profiles PC3 and PC4, concentrations of small particles (<1.5 mm) increased, whereas concentrations of large particles decreased. The following day (PC4 to PC5) particle concentration decreased with no further change in particle size distribution, but the BNL thickened (extended further upward). The associated salinity profiles (**Figure 4f**), T/S diagrams (**Figure 4g**), and temperature profiles (**Figure 4h**) reveal that the change in particle size distributions did not parallel a clear shift in water mass. Both temperature and salinity remained relatively unchanged over time.

Flux camera

Settling speed and size of marine snow measured at 80 mab varied appreciably on scales of hours to days, as well as between both sites. At OC26 the average settling speed of the marine snow, which had a mean estimated spherical diameter (ESD) of 0.88 ± 0.22 mm (n = 2,176), was 31

± 23 m d^{-1} during period 1; during period 2, the average settling speed of the particles, with a mean ESD of 0.75 ± 0.22 mm, was 35 ± 22 m d^{-1} (n = 1,436) (**Figure 5**). At GC600, settling marine snow had a mean ESD of 0.78 ± 1.5 mm and mean measured settling speed of 42 ± 22 m d^{-1} (n = 2,431). While the average ESD of marine snow was similar at both sites, settling speed was consistently higher at GC600 compared to OC26, although this difference was not statistically significant because of the high variability within each site (t test).

Settling speeds averaged over the time periods matching the collection periods of the co-located traps reveal that average settling speeds were loosely correlated with marine snow size (ESD) and with mineral content
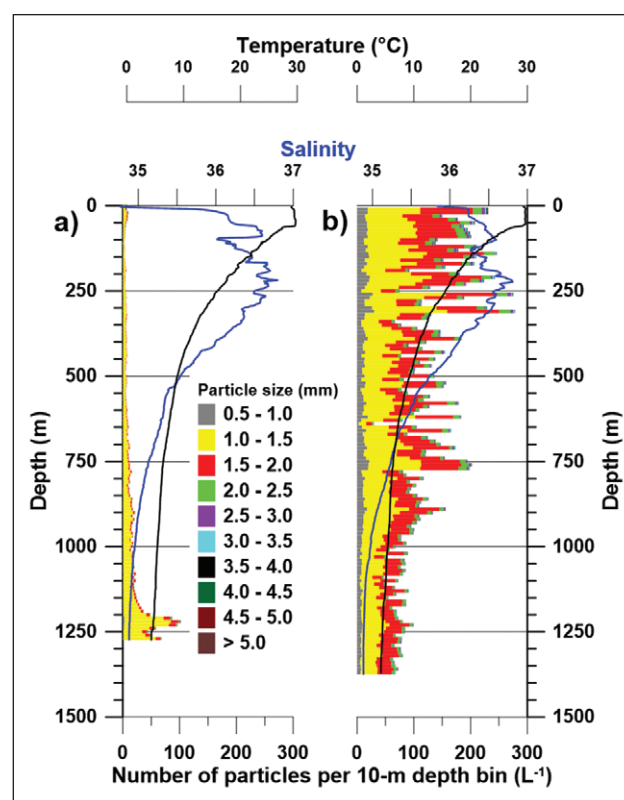

Figure 3: Profiling camera casts PC1 (left) and PC2 (right) at site GC600 during the EN515 cruise. Ten-meter vertically binned size-specific particle concentrations are plotted, according to the color scheme indicated for particle size (mm), together with vertical profiles of temperature (black line) and salinity (blue line). DOI: https://doi.org/10.1525/elementa.285.f3

Table 5: Mean percent (± SD) concentration of marine snow per size class in the total water column and the BNL. DOI: https://doi.org/10.1525/elementa.285.t5

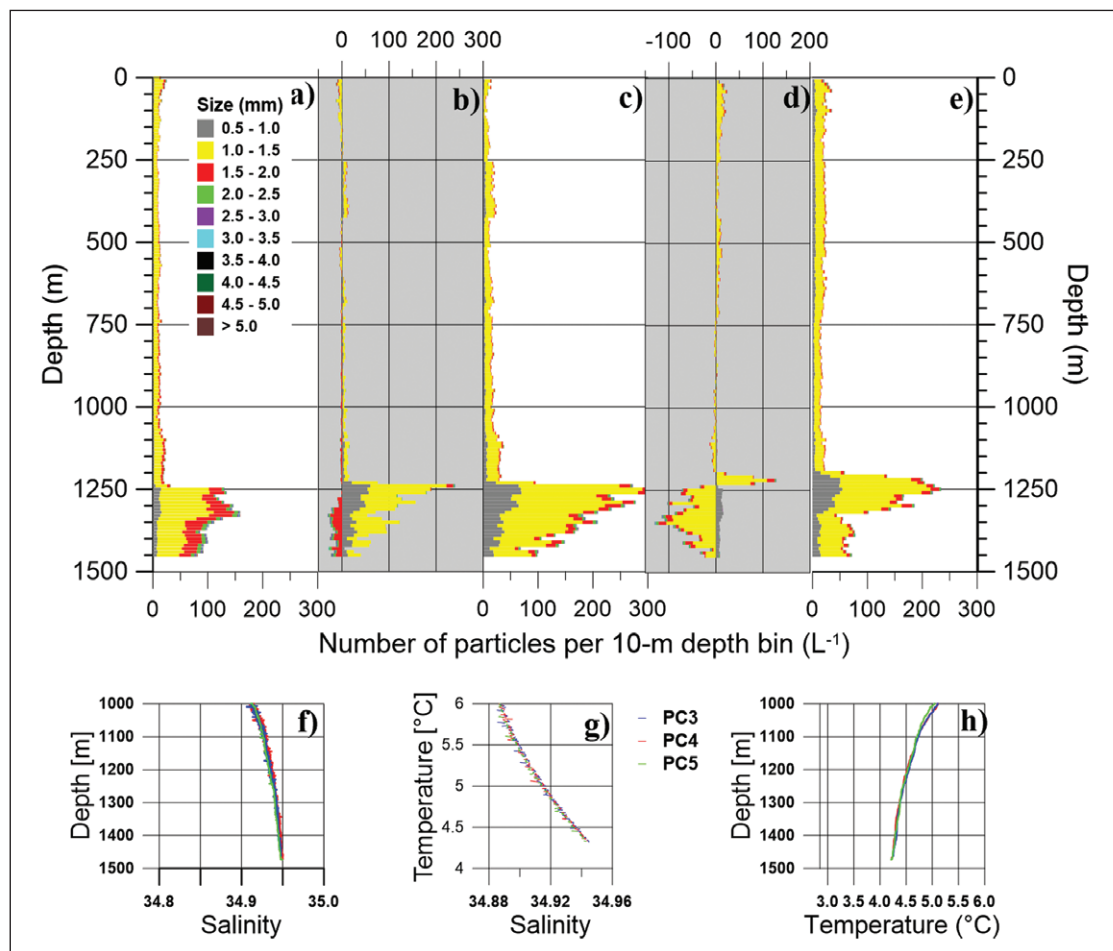| PC cast	Total water-column size class (mm)				BNL-only size class (mm)			
	0.5−1.0	1.0−2.0	2.0−4.0	n	0.5−1.0	1.0−2.0	2.0−4.0	n
1	4.20 ± 2.2	92.5 ± 4.5	3.1 ± 2.7	127	3.2 ± 0.5	93.6 ± 0.9	3.1 ± 0.5	3
2	10.1 ± 1.0	81.7 ± 1.6	8.0 ± 1.8	137	no BNL	no BNL	no BNL	N/A
3	9.9 ± 1.7	87.5 ± 2.1	2.3 ± 1.4	143	8.8 ± 1.2	82.9 ± 2.8	7.8 ± 3.2	21
4	20.4 ± 2.8	77.9 ± 2.7	1.6 ± 1.4	144	20.3 ± 3.0	76.8 ± 2.6	2.9 ± 1.2	22
5	21.8 ± 2.6	76.7 ± 2.7	1.4 ± 1.1	144	21.6 ± 3.0	76.6 ± 3.0	1.7 ± 1.0	26

Figure 4: Particle abundance profiles from profiling camera casts PC3 to PC5 with CTD data. Ten-meter verti-cally binned size-specific particle concentrations are plotted, according to the color scheme indicated for particle size (mm), for casts PC3 **(a)**, PC4 **(c)** and PC5 **(e)**, along with the changes in particle distribution between PC3 and PC4 **(panel b)**, and between PC4 and PC5 **(panel d)**. Strong changes below 1,300 m are visible with an apparent loss of particles >1.5 mm, even though total number of particles had increased. For all three camera casts, **panel f** presents salinity profiles, **panel g** depicts presents temperature versus salinity data, and **panel h**, presents the temperature profiles below 1,000-m depth. These data indicate that no changes in water mass had occurred. DOI: https://doi.org/10.1525/elementa.285.f4
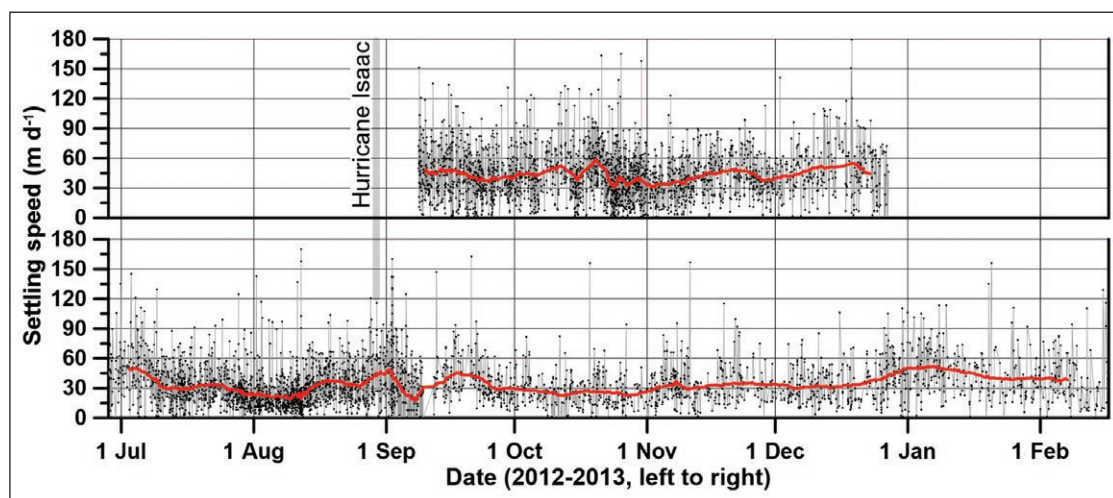
Figure 5: Marine snow sinking speed at sites GC600 (top) and OC26 (bottom). Black dots (connected by grey lines) indicate the sinking speed of each particle measured at GC600 and OC26. Red lines are 25-hour running aver-ages of the settling speeds. Black arrow and vertical grey bar near 30 August 2012 indicate the passage of Hurricane Isaac. The flux camera at GC600 stopped recording during the deployment in December of 2012. DOI: https://doi.org/10.1525/elementa.285.f5

of settling matter (**Figure 6**), though a multiple regression analysis revealed no significant overall correlation. The higher settling speeds at GC600 were associated with higher mineral and lower POC content, but variability was high during this time interval, obscuring the relationships.

Figure 7 presents in detail the variability of marine snow size and settling speed during the time period relevant for Hurricane Isaac. The diameter of marine snow increased on average from 0.8 mm ± 0.2 mm to 1.0 mm ± 3 mm (n = 76) on 31 August 2012, two days after Isaac made landfall on 29 August 2012. The variance in particle diameter was greatest during the peak in particle concentration, when the number of particles was counted in bi-hourly increments, on 2 September 2012 (Figure S1). A period
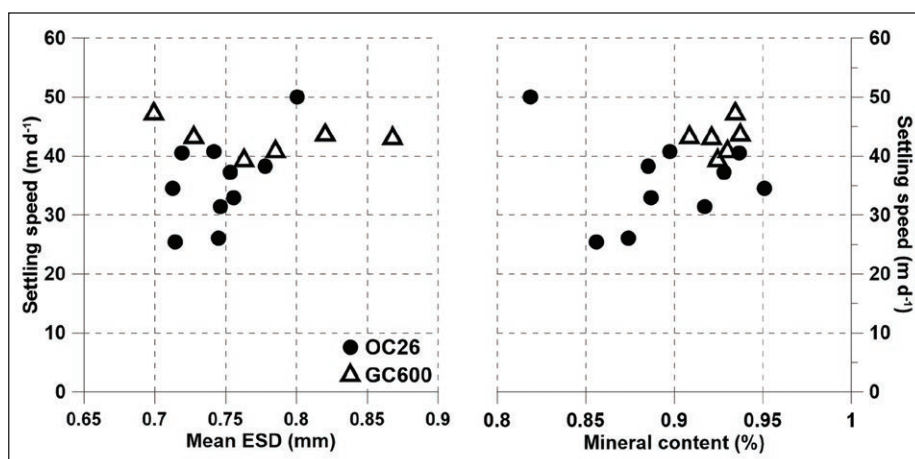
Figure 6: Particle settling speed versus mean equivalent spherical diameter and percent mineral content. Settling speed of particles versus equivalent spherical diameter (ESD) and percent mineral content from sediment trap data. Black dots represent data from the second trap deployment at OC26; triangles represent the available data at GC600. DOI: https://doi.org/10.1525/elementa.285.f6
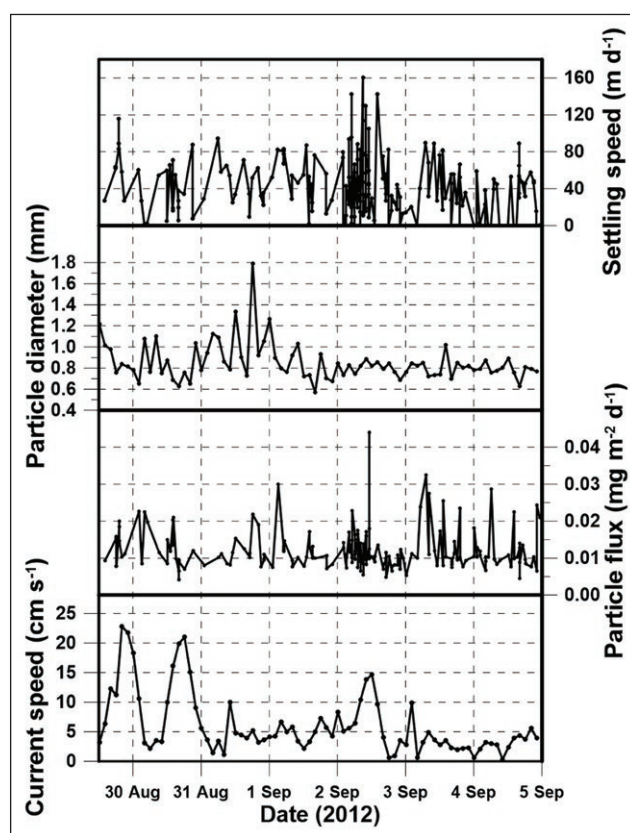
Figure 7: Passage of Hurricane Isaac documented in ADCP and flux camera data at OC26. Bi-hourly particle flux calculated as outlined in methods section using fractal equation by Maggi (2013) per individual particle. Numbers of particles arriving in the flux camera are reflected in the uneven spacing of data points along the x-axis. Particle settling speed, diameter and particle flux are plotted relative to the current speed. The two large peaks in current speed on 30 and 31 August are related to Hurricane Isaac passing over the mooring site. All dates are for the year 2012. DOI: https://doi.org/10.1525/elementa.285.f7

of low variance in ESD lasting at least 7 days (sampling period was interrupted during recovery of the mooring on 9 September 2012 and redeployment on 11 September 2012) followed the passage of Isaac. High variances in ESD characterized the days between 11 and 15 September, spanning the time of the three profiling camera casts PC3 to PC5, corroborating the observation of a short-lived resuspension event in those profiles as discussed below.

No simultaneous change in mean measured settling speed was observed at that time. However, 48 particles with a mean settling speed of 52 ± 42 m d^{-1}, with some speeds reaching 160 m d^{-1}, were measured at OC26 in a 12-hour period on 2 September between 04:00 and 16:00. During the same 12-hour time period before and after this event, 13 and 30 small and well sorted particles, respectively, were imaged by the flux camera as having settling speeds of $< 41 \pm 32$ m d^{-1} and $< 36 \pm 27$ m d^{-1} respectively.

Between 11 and 14 September, the time of PC3–PC5, no significant changes in mean particle ESD were noted; however, a hiatus in settling speed measurements occurred on 13 September 2012. During this day, no individual settling speeds could be resolved in the flux camera, due to the setup of the camera and the timing interval between the images. Individual particles were enumerated during 13 September, though they appeared only once in each image, indicating their presence and allowing us to determine a concentration. However, these particles moved too fast to be captured in subsequent images, resulting in no data for settling speeds. Mean particle ESD of 0.85 ± 0.04 mm (n = 49) during 13 September did not vary significantly from the days before and after. Bi-hourly concentrations dropped from 9 ± 3 L^{-1} (n = 107) on 12 September 2012 to 4 ± 2 L^{-1} (n = 49) on 13 September 2012, appearing to increase again to 5 ± 3 L^{-1} (n = 71) on 14 September 2012. Average settling speeds from noon to midnight on 12 December 2012 doubled from 18 ± 9 m d^{-1} (n = 8) to 38 ± 28 m d^{-1} (n = 8) before becoming too fast (e.g., >185 m d^{-1}) to be measurable on 13 September 2012. During 14 September, settling speeds decreased to 29 ± 9 m d^{-1} (n = 16).

Sediment traps

The vicinity of the Mississippi River leads to a high contribution of lithogenic silica (LSi) to the mass flux at OC26; e.g., on average $69 \pm 7\%$ of mass flux was due to LSi, which is consistent with other years and also reflects the composition of the sediments below the Mississippi plume (Giering et al., 2018). Sedimentation rates at OC26 are largely driven by regional hydrography and the Mississippi, which both impact biological production of particles as well as their lateral transport (Giering et al., 2018). LSi and dry weight (DW) fluxes at OC26 varied by more than an order of magnitude, between ~52 mg m^{-2} d^{-1} and almost 639 mg m^{-2} d^{-1} for LiS and between 0.5 and 1,006 mg m^{-2} d^{-1} for DW within a year (Tables S1–S3). Total flux at the more off-shore station GC600 was 50% lower than at OC26. GC600 is less directly influenced by the Mississippi, and the average contribution of LSi to mass flux lower ($61 \pm 15\%$), although hydrography (loop currents and spin off eddies) episodically carries material from the coast to this station (Liu et al., 2018).

The POC:DW ratio of settled material at OC26 ranged from 2.2% to 8.6% (average $4.3 \pm 1.4\%$; n = 3), with a higher average ratio of 4.5% in the upper trap compared to 4.0% in the lower trap. The average POC:DW flux at GC600 was lower at $3.3 \pm 0.7\%$ (n = 3), reflecting the more offshore, oligotrophic location of GC600.

At OC26 five time periods were identified as periods of interest with respect to possible resuspension signals; that is, periods when the LSi sedimentation rate was appreciably different between the upper and lower traps (**Figure 8**). During these five time periods, the condition
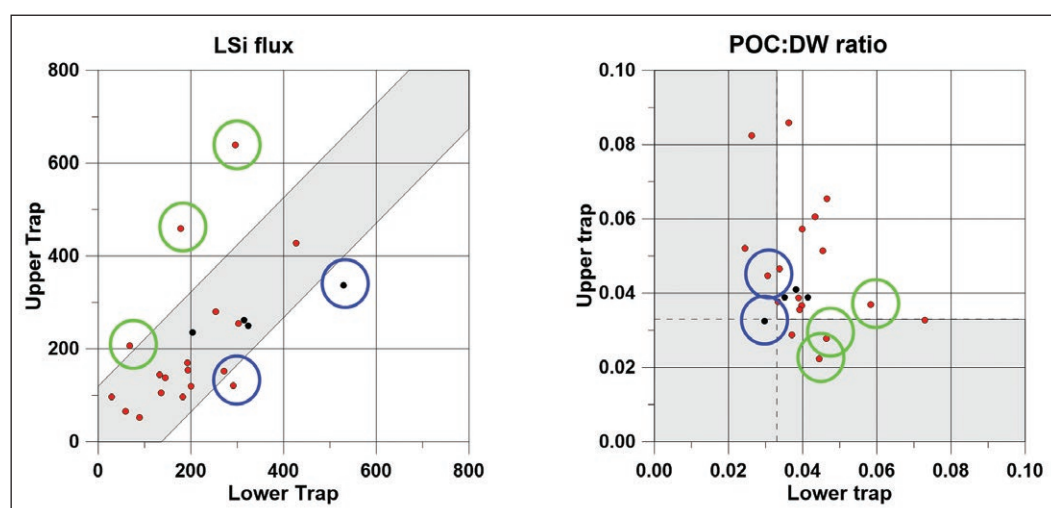

Figure 8: Classification of resuspension events. Values of LSi flux and POC:DW ratios at OC26 from the upper trap are plotted against the lower trap values, presenting two groups of sedimentation events. Green circles (sample cups 5, 11 and 15) are interpreted as far-field small resuspension events. Blue circles (cups 4 and 17) represent resuspension events with flux values of LSi$_{upper}$ $\ll$ LSi$_{lower}$, including large-scale hurricane events. In both panels, the black dots mark values from the first, and the red dots for the second, sediment trap deployment at OC26. The gray-shaded area in the left panel marks the sampling periods in which no clear resuspension signal was detected; the gray-shaded area in the right panel marks the condition for POC:DW being less than 3% in both traps. DOI: https://doi.org/10.1525/elementa.285.f8

Table 6: Potential resuspension events[a] at OC26 identified from two traps deployed at 30 mab and 120 mab. DOI: https://doi.org/10.1525/elementa.285.t6

Event	Event timing	Trap period and characteristics	Supporting evidence	Comments
Large-scale resuspension: Hurricane Isaac	28 Aug–2 Sept 2012	21 Aug–8 Sept 2012 (cup 4); $LSi_{upper} \ll LSi_{lower}$; $POC:DW_{upper} = 3.3$; $POC:DW_{lower} = 3.0$; $\delta^{34}S_{upper} = 15.5‰$; $\delta^{34}S_{lower} = 15.4‰$	High current speeds, especially at M2, 3, 4 and ADCP; high particle concentrations at 108 mab, as seen in ADCP; peak sinking velocities of very small particles on 2 Sept (flux camera); $\delta^{34}S_{upper} = \delta^{34}S_{lower}$	Hurricane Isaac caused high deep currents at the site on 28 Aug, making landfall on 29 Aug; water pushed back from shore gives a second signal at the site, 31 Aug to 2 Sept. Both events caused large-scale resuspension reaching to above 120 mab, impacting both traps, with more material entering the lower trap, suggesting most resuspended material came from below.
Small-scale resuspension	12–14 Sept 2012	8–29 Sept 2012 (cup 1, 2nd deployment); no $\delta^{34}S$ data	High current speeds, specifically at M3, M4; changes in BNL at PC3–PC5	Rapid changes were observed in the BNL: thickening of the BNL, changes in particle size distribution, initial increase in particle concentration followed by decrease associated with the increase in deep current speeds.
Far-field, small-scale resuspension/BNL	Nov–Dec 2012	21 Nov–8 Dec 2012 (cup 5); $LSi_{upper} \gg LSi_{lower}$; $POC:DW_{upper} = 2.2$; $POC:DW_{lower} = 4.4$	Current speeds at M3 low, <10 cm s^{-1}; no $\delta^{34}S$ data	This type of signal may best be explained by resuspension on higher lying slopes, with the formation of a deep nepheloid layer carrying resuspended material into the upper but not lower trap.
Far-field, small-scale resuspension	Mar 2013	5–22 Mar 2013 (cup 11); $LSi_{upper} \ll LSi_{lower}$; $POC:DW_{upper} = 3.7$; $POC:DW_{lower} = 5.8$	Current speeds at M3 elevated, >20 cm s^{-1}; $\delta^{34}S_{upper} = 15.8‰$; $\delta^{34}S_{lower} = 17.2‰$	Same as above
Far-field, small-scale resuspension/BNL	May 2013	13–31 May 2013 (cup 15); $LSi_{upper} \gg LSi_{lower}$; $POC:DW_{upper} = 2.8$; $POC:DW_{lower} = 4.6$	Current speeds at M3 low, <10 cm s^{-1}; no $\delta^{34}S$ data	Same as above
Local small-scale resuspension	June–July 2013	17 Jun–4 Jul 2013 (cup 17); $LSi_{upper} \ll LSi_{lower}$; $POC:DW_{upper} = 4.5$; $POC:DW_{lower} = 3.1$	Current speeds at M3 elevated, >10 cm s^{-1}; no $\delta^{34}S$ data	Resuspended material only entered lower trap, suggesting the nepheloid layer to be between 30 and 120 mab.

[a] A significant difference in LSi flux between the two traps (smallest deviation > 95 mg m^{-2} d^{-1}) and a POC:DW ratio ≤3.3 in at least one trap (Figure 8) was interpreted as an indicator of resuspension.

that POC:DW be ≤3.3% in at least one of the two traps was met four times: two times (November–December 2012 and May 2013), when an appreciably higher LSi flux rate was observed in the upper compared to the lower trap and a low POC:DW ratio (2.2 and 2.8) was observed in the upper trap; and another two times (September 2012 and June–July 2013) when the flux rate was appreciably higher in the lower trap than in the upper one, and a POC:DW ratio of < 3.3 was observed in the lower trap (July 2013) or in both traps (September 2012) (**Table 6**). March 2013 was not identified as a time period with a significant resuspension event, even though LSi flux in the upper trap was twice that in the lower trap, because the POC:DW ratio was 3.7, clearly above our criterion of 3.3.

Direct comparisons were made of the $\delta^{34}S$ of upper and lower sediment trap material for nine time periods (Tables S1 and S2). The $\delta^{34}S$ of the trap material varied from 19.7 to 13.2‰, indicating that the primary source of the sulfur was via assimilatory sulfate reduction of marine sulfate (20‰) by water-column primary producers, which occurs with little isotopic fractionation of sulfur (Rees et al., 1978). A source of ^{34}S-depleted sulfur to the traps could have been from sulfides produced by dissimilatory sulfate-reducing bacteria (Chanton et al., 1987), incorporated into either pyrite or organic matter, from either recent sediments or petrocarbon. Thus, variations in the $\delta^{34}S$ signature of sediment trap material may be interpreted as being affected by the relative importance of sulfur derived from marine primary production versus the input of sediment-derived sulfur or possibly organic matter derived from petrocarbon, which also may be affected

by sulfate-reducing bacteria. A lighter, ^{34}S-depleted signal indicates the increased relative importance of petroleum hydrocarbon input (Prouty et al., 2016; Yan et al., 2016) or resuspension of material. Both of these sources have been exposed to anaerobic conditions and dissimilatory sulfate reduction. On 16 July the lower trap was ^{34}S-depleted relative to the upper trap, and on five occasions the upper trap was ^{34}S-depleted relative to the lower trap (8 December 2012, 12 and 20 January, 15 February and 5 March 2013; Tables S1 and S2). These differences may be interpreted as the admixture of greater or lesser quantities of resuspended materials assuming that resuspended material had been exposed to more anaerobic conditions and the activities of sulfate-reducing bacteria. Measured ^{34}S values for both upper and lower traps were the same over three sampling periods, 26 June, 3 and 21 August 2012. The 21 August 2012 sampling cup included the passage of Hurricane Isaac. $\delta^{34}S$ values from 21 August 2012 and 5 March 2013 are corroborating resuspension events (**Table 6**) as discussed below.

Currents

Current meter data collected by the ADCP at OC26 and the single point current meters from the GISR moorings at M1 to M6 present episodes in current direction and magnitude that support our data observations which indicate resuspension events of different strength, from those driven by frequent inertial currents to the episodic high energy event triggered by Hurricane Isaac (**Figure 9**).

Current meter data collected over the entire deployment indicate that the meridional component dominated
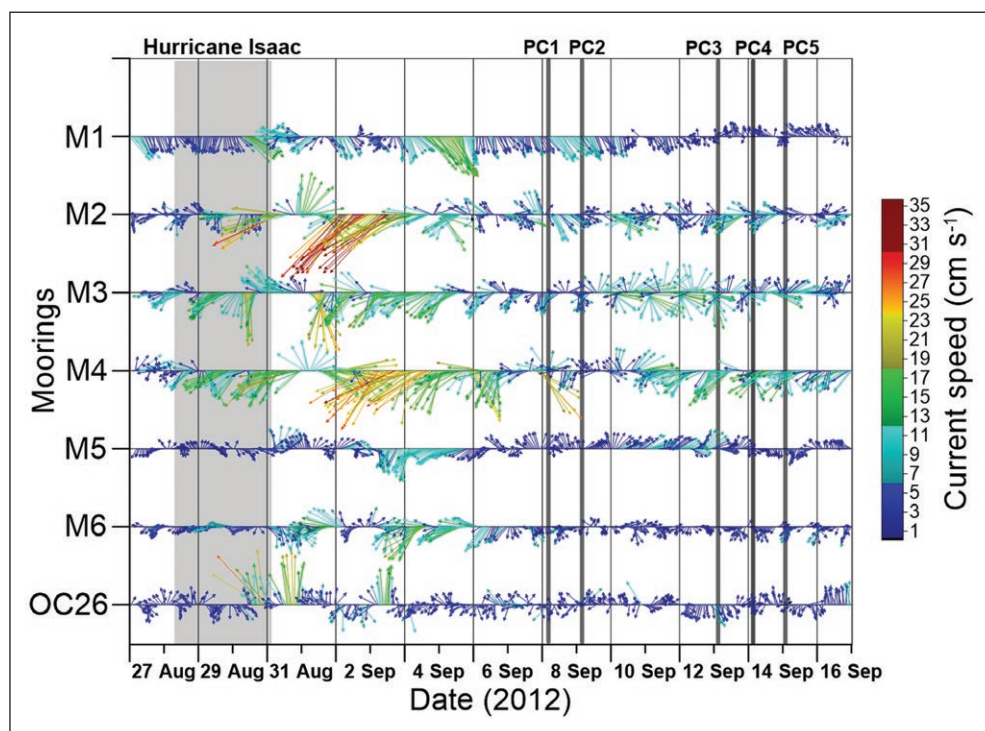

Figure 9: Current vectors at sites M1 to M6 and OC26, 26 August to 16 September 2012. Shaded grey box marks the period when Hurricane Isaac moved across the moorings. Vertical grey bars mark the times of the five different profiling camera casts. PC1 and PC2 are plotted for time reference only, as the current meters were moored spatially too far from these camera casts to be relevant. DOI: https://doi.org/10.1525/elementa.285.f9

the flow at OC26 (**Figure 10**). The ADCP data include the signal of the passage of Hurricane Isaac over the OC26 mooring on 28 August before making landfall on 29 August 2012. Current speeds near the seafloor at 1,633 m as measured with the ADCP increased to 23 cm s^{-1} on 29 August 2012; their direction rotated from north to south and back to north with the passage of the hurricane (**Figure 9**). After Isaac made landfall in the morning hours on 29 August, hurricane-force winds quickly diminished, allowing the water that was forced into the MS Bight to flow back offshore, carrying resuspended material off the shelf and slope out into the open ocean between 31 August and 2 September 2012. During the two days after the hurricane made landfall (29–30 August), currents transported water to the NNW in the bottom 100 m of the water column reaching 20–23 cm s^{-1}. The ADCP data also reveal that high particle concentrations reached especially far up above the seafloor on 2 September; e.g., at least 100 m above the ADCP or 108 mab (**Figure 9**).

Current speed and direction measured with the single point current meters at M1 to M6 between 27 August and 2 September 2012 also mirror the impact of Hurricane Isaac (**Figure 9**). The strong near-surface inertial response to the impulsive forcing of the hurricane is typical of hurricanes in the Gulf of Mexico (Brooks, 1983; Jaimes and Shay, 2010). Currents at M1, which showed a generally southerly tendency, changed to an east–west component during the passage of Hurricane Isaac. M2 measured the strongest currents on 1 and 2 September 2012.

A northward flow on 31 August 2012 was followed by two days of strong SSW currents reaching 35 cm s^{-1}. M3 recorded early currents moving water from east to west on 27–28 August 2012, followed by currents to the south which rotated through west to north during the hurricane passage, to again turn south after landfall of Isaac on 31 August 2012, staying for days in that same general direction (**Figure 9**). Strong SW currents started two days after the passage of the hurricane at M4 and one day at M2. M5 and M6 did not record any prevailing changes in current speed or direction associated with Hurricane Isaac's passing (**Figure 9**).

By 12–14 September, when the PC casts were completed, the current magnitudes at M1 to M3 were 6 to 12 cm s^{-1}, but strong variations in directions between the three moorings were recorded (**Figure 9**). M1 recorded a flow to the south from 7 September to early 11 September, which turned to a northerly flow until 13 September, followed by a few hours of southerly flow. By early 14 September, the currents returned back towards the north. M2 and M3 recorded clockwise inertial currents with magnitudes varying between 3 and 16 cm s^{-1} (**Figure 9**). Currents recorded with the ADCP at the sediment trap mooring flowed to the north following the passage of Hurricane Isaac over the mooring site early 30 August to early 1 September 2012. A day of southward currents during 1 September to early 2 September was followed again by strong currents reaching 14–16 cm s^{-1} during the day of 2 September 2012. Current speeds and directions returned
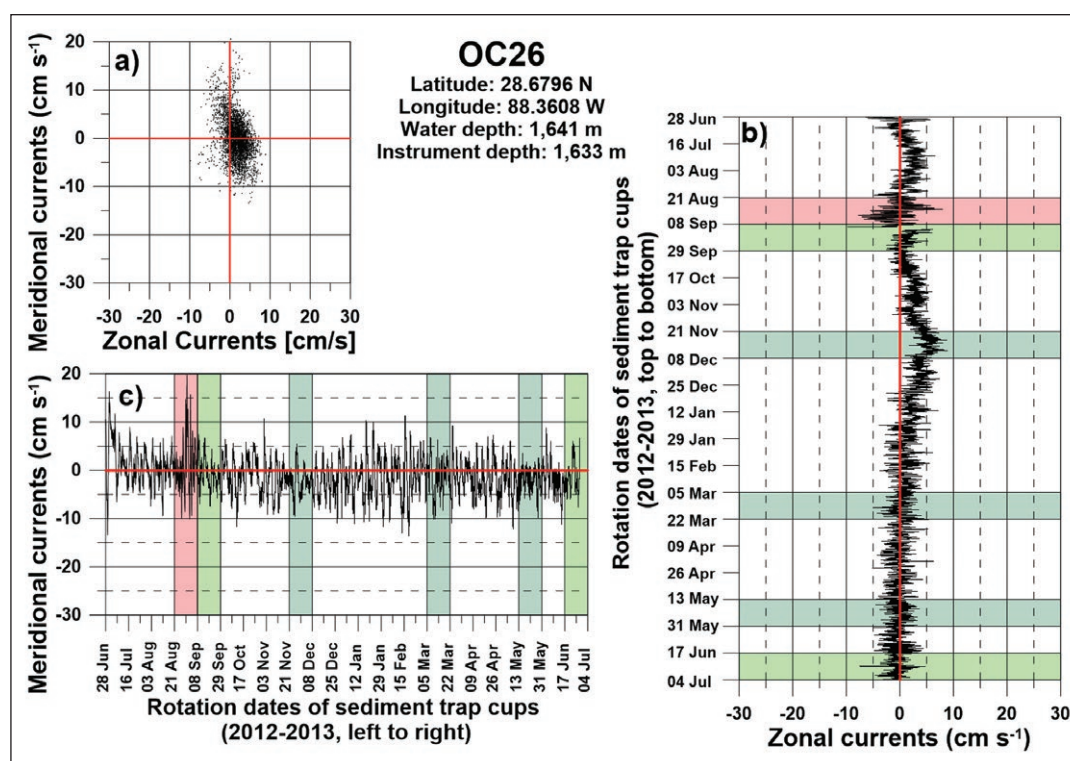

Figure 10: Zonal and meridional flow at the sediment trap mooring site OC26. Panel **a)** presents zonal versus meridional flow at the site from 28 June 2012 to 4 July 2013, covering the sediment trap deployment period. Panel **b)** displays the hourly meridional flow of the measured currents and panel **c)**, the zonal currents. Time intervals are marked corresponding to the lower trap schedule, with a new cup rotating under the collecting funnel at the start of each interval. The red bar indicates a large-scale resuspension event. Light green bars mark the collection interval that sampled small-scale resuspension events in the near field; dark green bars mark the collecting periods that correspond to the far-field small resuspension events of Table 6. DOI: https://doi.org/10.1525/elementa.285.f10
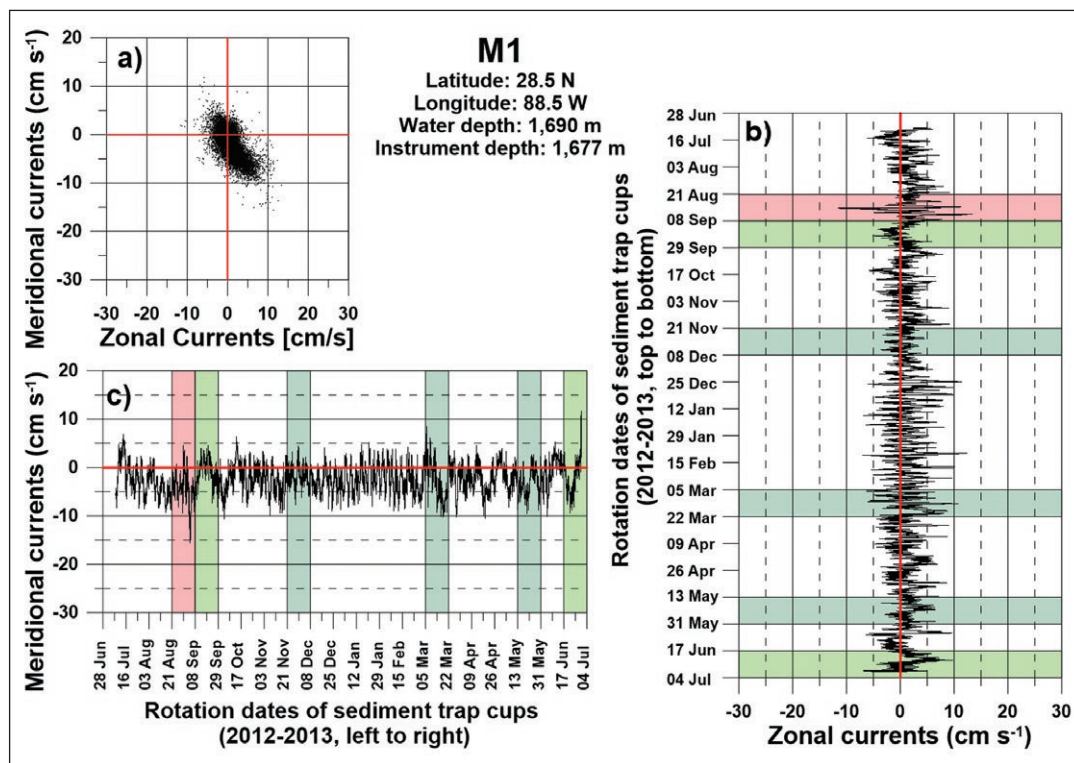
Figure 11: Zonal and meridional flow at GISR Mooring site M1. Panel **a)** presents zonal versus meridional flow at the site from 28 June 2012 to 4 July 2013, covering the sediment trap deployment period. Panel **b)** displays the hourly meridional flow of the measured currents and panel **c)**, the zonal currents. Time intervals are marked corresponding to the lower trap schedule, with a new cup rotating under the collecting funnel at the start of each interval. The red bar indicates a large-scale resuspension event. Light green bars mark the collection intervals that sampled small-scale resuspension events in the near field; dark green bars mark the collecting periods that correspond to the far-field small resuspension events of Table 6. DOI: https://doi.org/10.1525/elementa.285.f11

to pre-hurricane conditions on 3 September 2012, exhibiting 2–6 cm s^{-1} from varying directions until 11 September when a prolonged period of two days of constant southerly currents were recorded with stronger currents early on 12 September reaching 6–8 cm s^{-1}. During the two days following this southerly flow, currents below 6 cm s^{-1} varied between north and south, then increased again on 15 September to stronger currents from the south reaching 8–12 cm s^{-1}. These lower current speeds compared to the ones during and immediately after Isaac, and the high variability in current direction, suggest the dominance of different, spatially small resuspension events with the currents in mid-September (**Figure 10**).

The deployment location of the sediment trap is close to the critical latitude of 30°N, where the local inertial period is approximately 24 h, which is very near to the local diurnal tidal period (DiMarco et al., 2000; Zhang et al., 2009, 2010). Therefore, the oceanic response is generally inertial with elements of a sub-inertial coupling at periods of about 2–4 days and 5–12 days (Spencer et al., 2016). Relative vorticity prior to the passage of Hurricane Isaac was reported as strongly negative on the right side of the hurricane, while positive on the left side. Spencer et al. (2016) reported an observed shift to slightly larger inertial frequencies of ~1.11 f and verified this shift theoretically. A propagation of this energy of 5.7 km d^{-1} horizontally and 29 m d^{-1} vertically was estimated.

Meridional currents similar to those observed at OC26 were measured at M1 (**Figure 11**), whereas currents at M2 (**Figure 12**) were dominated by zonal flow with a net transport to the south and west of the mooring site. Inertial currents near the seafloor with speeds >10 cm s^{-1} were recorded at M3 (**Figure 13**) on several other occasions, especially clearly in March 2013 and June–July 2013, indicating the possibility of local resuspension events. June–July 2013 was identified as a period when the lower trap, but not the upper trap, showed a resuspension signal, but trap data do not support the idea of a local resuspension event in March 2013. In November–December 2012 and in May 2013, the two periods identified as times of small-scale, far-field resuspension events based on trap comparisons, current speeds at M3 were below 10 cm s^{-1}. Zonal and meridional currents for GISR moorings M4 to M6 are presented in Figures S4–S6.

To estimate resuspension potential and compare our reported current meter data to published literature values, bed shear stresses were calculated for the height of the current meter above the seafloor for moorings at OC26 and M1 to M3 and are presented in **Figures 14−17** and Figures S7–S9 for M4 to M6. Current meters on moorings M5 and M6 were deployed at 200 mab. Bed shear stress values for these sites were calculated, but only to present trends in the data.

Discussion

Our profiling camera data demonstrate that while a BNL is not continuously present in the northern Gulf of Mexico, it is a frequently occurring phenomenon in this area. In
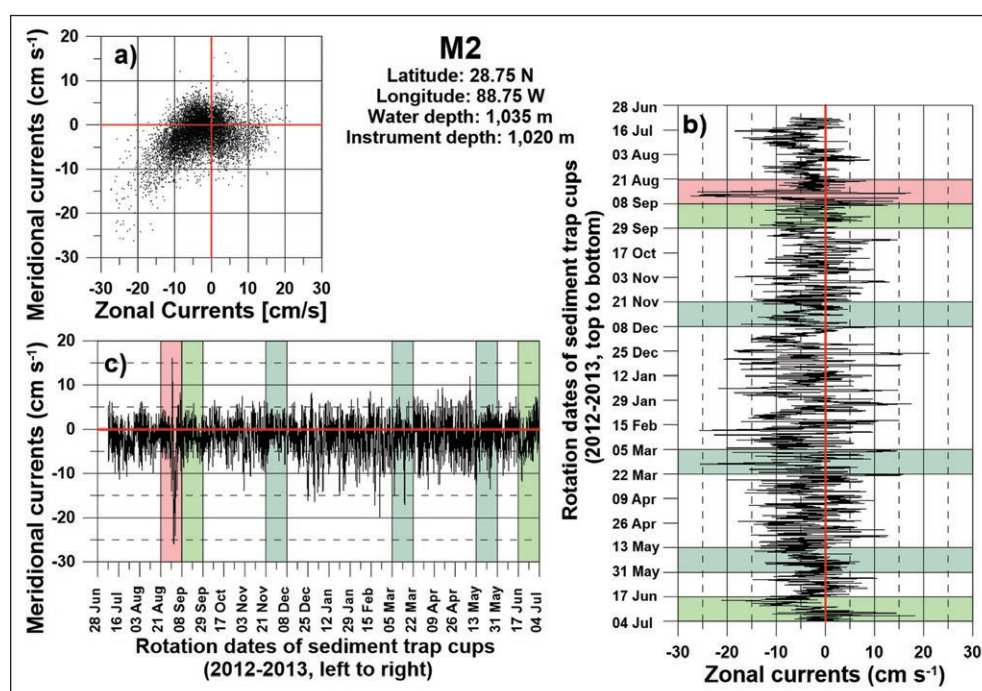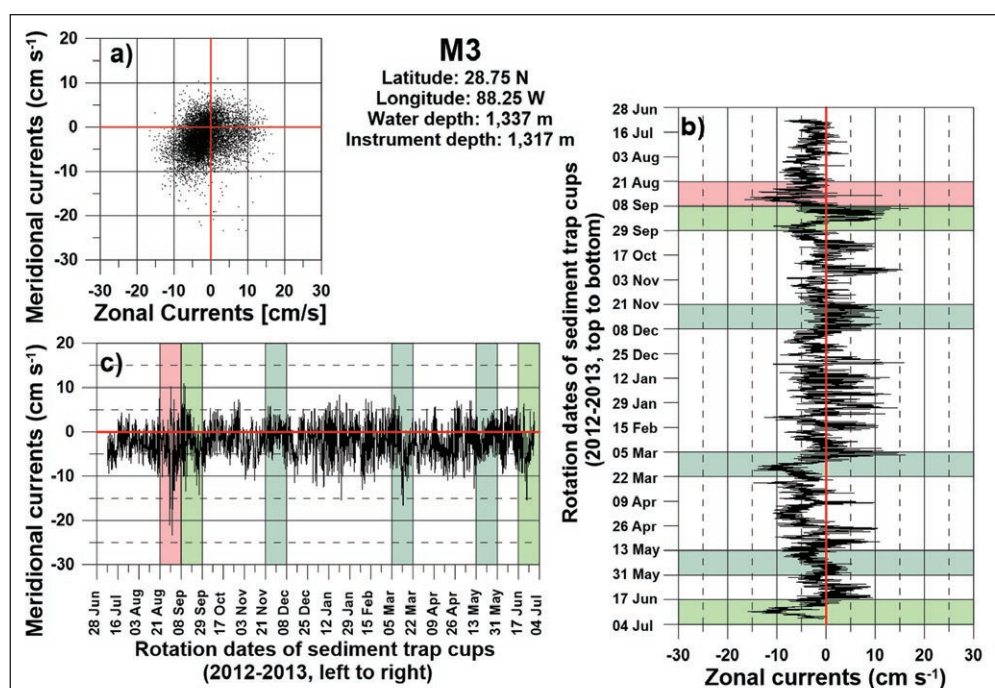
Figure 12: Zonal and meridional flow at GISR Mooring site M2. Panel **a)** presents zonal versus meridional flow at the site from 28 June 2012 to 4 July 2013, covering the sediment trap deployment period. Panel **b)** displays the hourly meridional flow of the measured currents and panel **c)**, the zonal currents. Time intervals are marked corresponding to the lower trap schedule, with a new cup rotating under the collecting funnel at the start of each interval. The red bar indicates a large-scale resuspension event. Light green bars mark the collection intervals that sampled small-scale resuspension events in the near field; dark green bars mark the collecting periods that correspond to the far-field small resuspension events of Table 6. DOI: https://doi.org/10.1525/elementa.285.f12
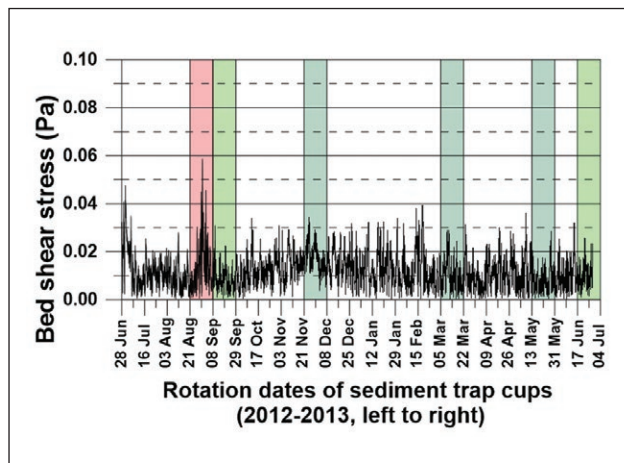

Figure 13: Zonal and meridional flow at GISR Mooring site M3. Panel **a)** presents zonal versus meridional flow at the site from 28 June 2012 to 4 July 2013, covering the sediment trap deployment period. Panel **b)** displays the hourly meridional flow of the measured currents and panel **c)**, the zonal currents. Time intervals are marked corresponding to the lower trap schedule, with a new cup rotating under the collecting funnel at the start of each interval. The red bar indicates a large-scale resuspension event. Light green bars mark the collection intervals that sampled small-scale resuspension events in the near field; dark green bars mark the collecting periods that correspond to the far-field small resuspension events of Table 6. DOI: https://doi.org/10.1525/elementa.285.f13
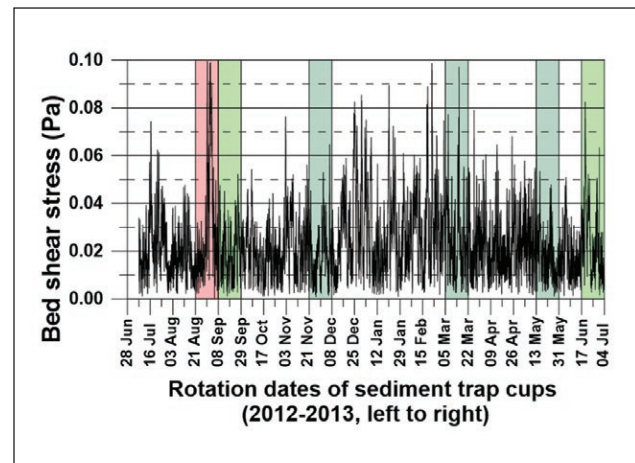
Figure 14: Bed shear stress at sediment trap mooring site OC26. OC26 bed shear stress was calculated using actual current measurements, kinematic viscosity of seawater at 4°C, and the height of the first bin of the ADCP measurement (18 mab). Time intervals are marked corresponding to the trap schedules, with a new cup rotating under the collecting funnel at the start of each interval. The red bar indicates a large-scale resuspension event. Light green bars mark the collection intervals that sampled small-scale resuspension events in the near field; dark green bars mark the collecting periods that correspond to the far-field small resuspension events of Table 6. DOI: https://doi.org/10.1525/elementa.285.f14
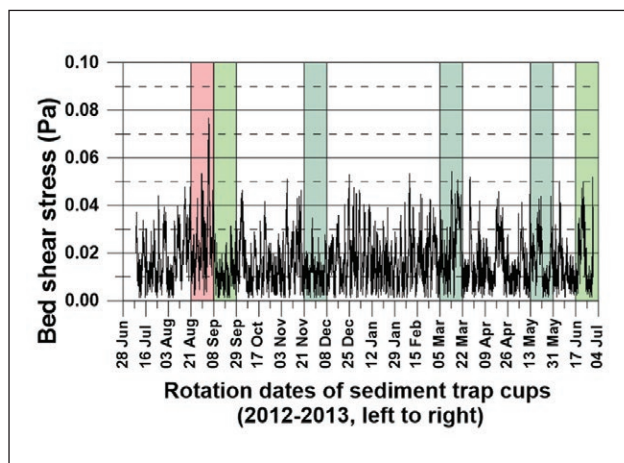

Figure 16: Bed shear stress at mooring site M2. M2 bed shear stress was calculated using actual current measurements, kinematic viscosity of seawater at 4°C, and the height of the single point current meter above the seafloor (15 mab). Time intervals are marked corresponding to the trap schedules, with a new cup rotating under the collecting funnel at the start of each interval. The red bar indicates a large-scale resuspension event. Light green bars mark the collection intervals that sampled small-scale resuspension events in the near field; dark green bars mark the collecting times that correspond to the far-field small resuspension events of Table 6. DOI: https://doi.org/10.1525/elementa.285.f16
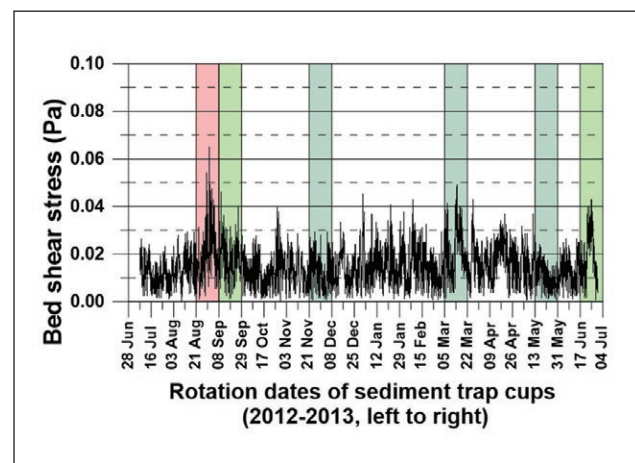

Figure 15: Bed shear stress at GISR mooring site M1. M1 bed shear stress was calculated using actual current measurements, kinematic viscosity of seawater at 4°C, and the height of the single point current meter above the seafloor (13 mab). Time intervals are marked corresponding to the trap schedules, with a new cup rotating under the collecting funnel at the start of each interval. The red bar indicates a large-scale resuspension event. Light green bars mark the collection intervals that sampled small-scale resuspension events in the near field; dark green bars mark the collecting periods that correspond to the far-field small resuspension events of Table 6. DOI: https://doi.org/10.1525/elementa.285.f15

Figure 17: Bed shear stress at mooring site M3. M3 bed shear stress was calculated using actual current measurements, kinematic viscosity of seawater at 4°C, and the height of the single point current meter above the seafloor (20 mab). Time intervals are marked corresponding to the trap schedules, with a new cup rotating under the collecting funnel at the start of each interval. The red bar indicates a large-scale resuspension event. Light green bars mark the collection intervals that sampled small-scale resuspension events in the near field; dark green bars mark the collecting periods that correspond to the far-field small resuspension events of Table 6. DOI: https://doi.org/10.1525/elementa.285.f17

23 profiles spanning 5 years we observed a BNL 21 times (**Table 1**). Sediment resuspension events occur from all depths of the seafloor and in a variety of environments, including large lacustrine environments (Valipour et al., 2017), and coastal and deep open ocean areas (Gardner, 1978; Gardner et al., 1984, 1985, 2017; Walsh et al., 1988; Bonnin et al., 2002, 2005, 2006; Bonnin, 2004; Puig et al., 2004, 2012, 2013; Peine et al., 2009; Ross et al., 2009). Benthic nepheloid layers formed by erosion and resuspension of material from the seafloor are thus also found at all depths in the world ocean. The formation of a deep BNL was recorded in our camera data, and the subsequently observed change over time in particle size distribution within that layer we attribute to lateral advection, similarly to the formation of nepheloid layers, observed in less than 70 m of water depth in the Baltic Sea, which reportedly moved along haloclines as intermediate nepheloid layers and contributed through lateral advection to the deposition of material in the deeper portions of the Baltic Sea (Tamelander et al., 2017). Wilson (2016) described the occurrence of BNLs in the Celtic Sea along the NE Atlantic continental margin down to 2,500 m water depth, and found intermediate nepheloid layers (INLs) to be extensions from their benthic shelf and slope sources, reaching 25 km offshore.

BNLs, as layers of high turbidity and particle concentration directly above the seafloor, are frequently formed due to seafloor erosion by strong bottom currents (Gardner et al., 2017). Flow at around 40 cm s^{-1} appears to initiate the transport of sediment proper in a BNL, whereas much lower speeds (e.g., 7–20 cm s^{-1}) resuspend fluffy aggregates (rebounded material; Walsh et al., 1988; Gardner and Walsh, 1990) into the BNL (Bonin et al., 2002, and citations therein). Turnewitch and collaborators (2017) and Emeis et al. (2002) showed that current speeds as low as 5–10 cm s^{-1} may impact the formation of BNLs. Emeis et al. (2002) attributed the resuspension at such low current speeds to the fluffy material overlying nearshore sandy sediments in the Baltic Sea. In this study, currents observed near the OC26 mooring during the local resuspension events ranged from 5 to 11 cm s^{-1}, but were unrelated to the measured particle flux during times when resuspended material originated in the far field (**Figure 10**).

Besides current speed, variability in higher frequency tidal or near-inertial current direction may also act as a controlling factor in the formation and occurrence of BNLs and INLs (Turnewitsch et al., 2013). Variations in topographically driven flow fields around seamounts have been shown to lead to strongly asymmetric flow around deep seamounts, similar in shape and size to those in the vicinity of the OC26 mooring. These asymmetric flow patterns in turn lead to uneven sedimentation dynamics affecting erosion, resuspension, deposition and sedimentation (Peine et al., 2009; Turnewitsch et al., 2013). Turnewitsch et al. (2017) suggest that the temporally and vertically varying rotational behavior of tidal and near-inertial flow translates into varying turbulence intensities; this turbulence plays a role in particle aggregation, resuspension and settling near the seafloor at current speeds

as low as <10 cm s^{-1}. Rotational currents were clearly observed at the M3 mooring (**Figure 18**), followed by lateral advection of material potentially resuspended by these events.

Turnewitsch et al. (2017) and Bonin et al. (2002, 2005) incorporated the differentiation of "resuspended" material, as in Walsh et al. (1988) and Gardner and Walsh (1990), distinguishing between particles that were deposited on the seafloor for some time and younger and lighter "rebounded" material that was only transiently in contact with the seafloor. In our investigation, the observed material during the small-scale resuspension events was predominantly rebounded material, based on the low current speeds associated with these events leading to the resuspension to the lighter, fluffy material only. In contrast, both resuspended and rebounded particles were introduced into the water column during the large-scale resuspension events, based on the increased LSi flux relative to POC. However, as our analysis was not focused on this distinction, the term "resuspended" particles will be used for all events in the remainder of this discussion.

Resuspension events, or benthic storms, are difficult to sample and identify, in part because they occur over a wide range of scales and are often sporadic. Bonnin (2002, 2005) used compositional data from stacked sediment traps moored 2 and 30 mab and co-deployed with current meters to identify resuspension events and the origin of the material collected in the traps. Their careful analysis of trap samples positioned along the shelf slope, allowed them to identify deposition zones where resuspension events were likely, and areas were resuspension was rare, as well as determine the origin of the collected material. One useful identifying parameter was the relative concentration of organic versus total flux. Using a similar approach, Tesi et al. (2012) reported that resuspension events from flat-topped summits of the Pacific Antarctic Ridge in the Antarctic Polar Front of the Southern Ocean accounted for 60 to 90% of the material captured in sediment traps deployed below. The presence of benthic foraminifera and significant higher ^{210}Pb activity indicated the presence of material originating from the seafloor. We combined a slightly modified approach of using stacked sediment traps with marine snow profiles and sinking velocity determinations of marine snow in the BNL to identify resuspension events.

Settling speeds as indicators of resuspension

Data from the flux cameras reveal that settling speeds of marine snow varied widely between 1 and >185 m d^{-1} with higher mean measured speeds at GC600 than at OC26. Only speeds < 185 m d^{-1} were resolvable with our system. The efficiency of capturing settling particles on more than a single image during the flux camera deployments weas between 2% and 68%. Our measured values compare well with the lower end of published values of settling marine snow (Asper, 1986; Alldredge and Silver, 1988; Diercks and Asper, 1997; Passow et al., 2012; Dike, 2015). As average particle size differed little between the two sites, differences in packaging or density of component particles must be responsible (De La Rocha and

Passow, 2007; Iversen and Ploug, 2010). The lower POC:DW ratio at GC600 compared to OC26 suggests that mineral particles contributed more to settling particles at GC600, suggesting higher excess density of settling marine snow. Moreover, the fraction of $CaCO_3$ in flux at GC600 is, on average, higher than at OC26, where lithogenic minerals contributed more to the flux (Giering et al., 2018). Calcium carbonate is thought to sediment organic matter more efficiently than most other minerals, because of its high excess density (Klaas and Archer, 2002). The observed differences in settling speed may thus be caused largely by differences in the composition of material exported from the upper ocean.

However, resuspension from sediments, which introduces mineral-rich material into the water column above the seafloor, also leads to changes in the size and settling speed of marine snow in the BNL, because particle concentrations and characteristics change dynamically within BNLs: large aggregates break and re-aggregate, thus changing in size and settling speeds, as most particles in BNLs are in the size range of fine silt to clay (Gardner et al., 2017). When incorporated into aggregates, the additional minerals will lead to decreased size but increased density, both of which impact settling speeds (Hamm, 2002; Passow et al., 2014). The lower average POC:DW ratio of the flux at 30 mab compared to 120 mab is likely caused from more frequent resuspension at 30 mab, although degradation of POC during the additional 100-m descent would have contributed also. The highest settling speeds of small particles, compared to their average settling speeds, were observed on 2 September 2012, four days after the passage of Hurricane Isaac, giving another example of such incorporation of fine sediments into the aggregates in the BNL. Likely the high mineral content of resuspended material caused the high, size-normalized settling speeds of marine snow in the BNL at that time. However, changes in settling speeds of marine snow in the BNL due to resuspension of mineral-rich material are frequently if not mostly obscured by variation in the settling speed of marine snow settling from the surface ocean.

Small-scale resuspension events
A local resuspension event caused by inertial currents near OC26 presumably produced the high LSi flux combined with low POC content observed in the lower trap, but not in the upper trap in June–July 2013 (**Table 6**). Resuspension events due to inertial currents are manifested in the formation of < 100-m thick BNLs. The strong currents (>10 cm s⁻¹) near OC26, which moved water from the east-northeast to the west-southwest as measured by the M3 current meter, substantiate the idea that this resuspension event occurred locally. Such a local or near-field event is expected to contribute only to the flux in the lower trap and not the upper trap, because the BNL would not reach to 120 mab.

The influence of seafloor morphology on material source to the mooring site at OC26 is demonstrated in **Figure 18** (and Figure S10). The diagram displays the potential source areas based on 18-day periods corresponding to the sediment trap schedule of the lower trap at OC26. For this

diagram, 18 days of hourly current vectors of M1, M2, M3 and OC26 current meters were plotted as vector additions starting at the current meter location, with each subsequent current vector starting at the end of the previous one. To highlight the material sources and the transport of material by the currents toward the sediment trap, the vectors (white lines in **Figure 18**) for the OC26 data were plotted as current flow toward the sediment trap. The origins of the white lines ending at OC26 are thus indicating the variety of source areas for material introduced by potential resuspension, which the trap samples would collect and which would add to the variability of material contributing to the flux, highlighting the difficulty of a simple classification of source material and origin over time. Current vectors from the M1, M2 and M3 moorings, displayed in **Figure 18**, present the variability of the current flow near the seafloor based on depth and location on the slope, but also clearly indicate that a local (small circles in the current lines) and a general westward transport (longer straight sections in the current meter vector data) of material eroding from the top and flanks of the domes surrounding the OC26 mooring is a valid option.

The changes in particle distribution in the BNL observed by PC3 to PC5 near OC26, along with the changes in particle size and the rapid settling of material on 13 September 2012, measured by the flux camera, and the respective current measurements, all suggest that another local, small-scale resuspension event occurred around 12–14 September 2012 (**Table 6**). This event was not visible individually in the trap, as it was obscured by the larger scale resuspension caused by Hurricane Isaac (see below) that took place within the same trap collection period. Camera casts PC3, PC4 and PC5 (**Figure 4**), however, recorded an increase in particle concentration below ~1,250 m and changes in size distribution, when temperature and salinity profiles do not suggest a change in water masses. Local near-inertial currents speeds of 8–16 cm s⁻¹ (**Figure 10**) were high enough to cause resuspension (Ziervogel et al., 2016; Gardner et al., 2017). Lampitt (1985) and Ziervogel and Bohling (2003) reported near-seafloor current velocities of ~6.5 to 10.5 cm s⁻¹ as sufficient to erode and resuspend sediment in the Porcupine Abyssal Plain and the southwest Baltic Sea, respectively. Klein and Mittelstaedt (1992) reported deep-sea benthic storms for the abyssal Atlantic with current speeds up to 27 cm s⁻¹ producing nepheloid layers.

Differences between PC3/PC4 and PC4/PC5 clearly highlight first an increase in particle concentration and thickness of the BNL, followed by a decrease in the depth range of the initial particle maxima and a change in particle size distribution, with fewer large particles in the BNL. In PC5 the particle layer had thickened by approximately 50 m upward in the water column. Highest particle concentrations, which were about 3 times higher than near the seafloor, were found in PC5 between ~1,200 m and 1,350 m. These changes in the particle size spectrum and settling speed of particles in the BNL suggest that a resuspension event introduced mineral-rich material from the seafloor into the water column, leading to re-aggregation. Size spectra within the BNL changed to overall
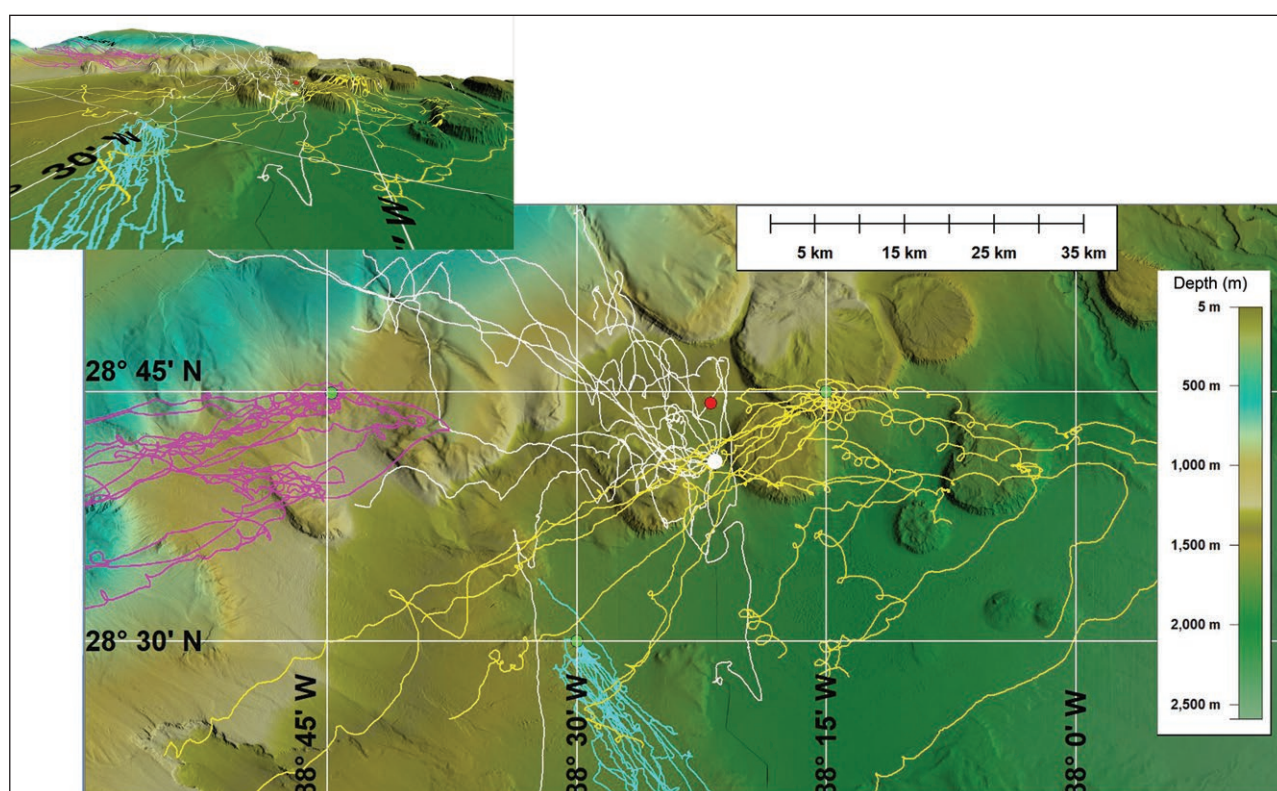
Figure 18: Diagram of current flow at selected mooring locations displayed as vector additions of 18-day periods. Blue, magenta and yellow lines centered on light green dots, represent 18-day periods of measured currents coinciding with the collecting periods of the sediment trap schedule at the GISR mooring sites M1, M2 and M3, respectively. Currents are presented as vectors originating at the mooring locations. White lines are 18-day periods of currents measured by the ADCP mounted near the seafloor at the sediment trap site OC26 (white dot). The current vectors at OC26 represented by white lines are calculated as "flow-towards" the mooring site to highlight the potential origins of resuspended material that was collected at the trap location. DOI: https://doi.org/10.1525/elementa.285.f18

smaller sizes (**Figure 4**) between PC3 and PC4, and settling speeds increased. All recorded particles during 13 September 2012 (PC4) settled at a minimum speed of 185 m d^{−1} (Figure S2). After approximately 24 hours the particle distribution in the BNL below 1,350 m exhibited similar characteristics as during PC3 (**Figure 4**), and particle settling speeds of < 185 m d^{−1} were recorded.

Variance in particle ESD, used as an indicator for aggregation and disaggregation of particles, was higher in the three camera profiles PC3 to PC5 than during the passage of Hurricane Isaac (Figure S1), suggesting resuspension of material from the seafloor by strong currents. Corroborative evidence of such small-scale local resuspension is presented by a pair of sediment trap samples that were [34]S-depleted in the lower trap relative to the upper trap (cup 2 first deployment, 16 July 2012; Tables S1 and S2). These data indicate that during this sampling period the vertical flux generated within the BNL, potentially by small-scale local resuspension, was relatively greater than at other times. Following a period of high variance in the particle size spectrum (ESD) during the passage of Hurricane Isaac, with its highest value on 2 September 2012, particle size distribution was the lowest, compared to the days before the hurricane passed over the mooring and the days following the camera casts PC3 to PC5 (Figure S1), indicating a well-mixed particle

size distribution. Variance in settling speed (Figure S3) is biased due to the missing speed data for the particles with only assumed minimum settling speeds.

In contrast to the local resuspension events, similar small-scale events, but at some distance and at shallower depths, result in a different signal when comparing the sample material from the traps at OC26. The POC:DW ratio of settled material at OC26 ranged from 2.2% to 8.6% (average of 4.5% ± 1.7%, n = 21), with a higher average ratio of 4.5% in the upper compared to 4.0% the lower trap. The average POC:DW flux at GC600 was lower at 3.3% ± 0.7% (n = 13), reflecting the more offshore, oligotrophic location of GC600. Our ratio of POC:DW agrees well with water column data recorded by Bonnin et al. (2002). They described organic carbon and nitrogen content of the trap samples as much lower in near-bottom sediment traps deployed in the deepest parts of the Faeroe-Shetland Channel, ranging from 10 ± 5.1% POC near the surface to 3.3 ± 1.2 and 3.9 ± 2.2% 5 mab at water depths of < 500 and 700 m, respectively, and 4.7 ± 2.2% at 700–900 m and 4.3 ± 2.0% at depths >900 m. A high flux event, captured in a sediment trap, depositing material with lower organic carbon and nitrogen values than collected during periods of low flux, was argued to be the result of increased input of sedimentary or resuspended material during that time.

Our analyses of the two stacked traps suggest that during November–December 2012 and May 2013 the upper trap collected material characteristic of resuspended material to a greater extent than the lower trap (**Table 6**). A greater heterogeneity in the collected material, attributed to resuspension events, was reported for traps moored at greater depth compared to shallow ones in a spatially and vertically separated sampling setup in Lake Michigan (Kerfoot et al., 2004). Sediment distribution, resuspension and transport are shown to be a function of the current flow-field and seafloor topography (Turnewitsch et al., 2004).

An additional indicator for small-scale far-field resuspension and lateral advection is offered by differences in $\delta^{34}S$‰ isotope concentrations between the two sediment traps at OC26. On five occasions the upper trap was ^{34}S-depleted relative to the lower trap (cups 6, 8, 9, 10, and 11 of the second deployment). Assuming that resuspended material had been exposed to more anaerobic conditions and the activities of sulfate-reducing bacteria resulting in depleted ^{34}S values, these differences may be interpreted as indicating that greater quantities of resuspended materials arrived in the upper trap than the lower trap. Lower or depleted ^{34}S would mean more relative sediment-affected material and more resuspension was captured by the trap.

We hypothesize that during these time periods, inertia-driven resuspension of material occurred in shallower areas surrounding the traps which subsequently was transported from those shallower water depths downslope, introducing this material as intermediate nepheloid layers to the trap site. Consistent with this idea, the currents near the OC26 site (M3) were <10 cm s^{-1} during the November–December and the May period suggesting no local resuspension. Such a short-scale intermediate nepheloid layer may have originated on the shelf or on the surrounding seamounts and advected laterally into the area. Settling particles from such an intermediate nepheloid layer may not reach the lower trap, because the INL could have moved onward before the material reached that depth. **Table 7** lists the mean total organic carbon concentration in surface sediments integrated over specific water-depth intervals. These data were downloaded in March 2013 from http://gulfsciencedata.bp.com/, a repository for the National Resource Damage Assessment sediment data. Concentrations of total organic carbon are at their highest between depths of 1,250 and 1,500 m, corroborating the source of material for local and far-field resuspension.

In summary, we suggest that small-scale resuspension events driven by inertial currents may appreciably impact transport and redistribution of lithogenic and organic sedimented material, both locally and in the far field. Especially in regions with varying topography, such events when occurring on a seamount or dome may carry matter farther afield, rather than sediment locally. Inertial resuspension events can last from hours to days. The frequency of the occurrence of these events is currently unknown; however, based on current meter measurements recorded by the M3 mooring, they could happen as frequently as daily, possibly sustaining a BNL in the form of pulsed material inputs. Such events may be imagined as high frequency "noise" on the seasonal curve of flux over time which is dominated by productivity, food webs, mesoscale circulation, riverine input and larger resuspension events.

Episodic large-scale resuspension events

The passage of Hurricane Isaac in August 2012 caused a larger scale resuspension event that was characterized by high energy and mass flux that lasted several days. Large storms are known to cause benthic storms at great depths (e.g., Gardner et al., 2017). Valipour et al. (2017) correlated maxima in ADCP signal amplitude to individual resuspension events in Lake Erie, similar to the event recorded at OC26 during the passage of Hurricane Isaac. Current meter data presented by Spencer et al. (2016) indicate propagation of near-inertial energy from Hurricane Isaac into the water column at M1, M3, and M4 affecting currents near the seafloor at >1,250 m water depth (**Figure 7**) and producing bed shear stress of 0.06 to 0.1 Pa and peak velocities of 23 cm s^{-1} at the current meter (**Figures 14−17**).

Critical bed shear stress of 0.02–0.03 Pa and current speed of 18 cm s^{-1}, measured at 10 mab, have been found sufficient to resuspend benthic fluffy material (Jago et al., 2002). Median current measurements of 6.0, 6.7 and 20.3 cm s^{-1} from three ADCP deployments at 1 mab in the northern Gulf of Mexico at Mississippi Canyon Block 118 (Martens et al., 2016) and Viosca Knoll Block 826, locations

Table 7: Total organic carbon concentration in the uppermost 1 cm of sediment cores from the northern Gulf of Mexico. DOI: https://doi.org/10.1525/elementa.285.t7

Depth range (m)	Total organic carbon (mg cm^{-3})[a]		Number of samples[b]
	Mean	Std. deviation	
0–500	no data	no data	no data
500–1000	0.747	0.217	55
1000–1250	0.857	0.249	211
1250–1500	0.947	0.376	320
1500–1750	0.792	0.308	215
>1750	0.765	0.323	104

[a] British Petroleum sediment data, downloaded March 2013 from Gulf Science data at http://gulfsciencedata.bp.com/, a repository for the National Resource Damage Assessment sediment data.

[b] Total of 905 individual samples, averaged into individual depth bins.

to the north and northeast of the OC26 mooring (Davies et al., 2010), resulted in bed shear stresses of 0.31, 0.35 and 1.06 Pa, respectively, all much higher than the 0.02–0.03 Pa range reported by Jago et al. (2002), confirming these areas as potential source areas for small-scale far-field and episodic large-scale resuspension events. Ziervogel and Bohling (2003) calculated critical shear stress velocities of 3.75 cm s^{-1} for cohesive muds, and presented results from laboratory analyses that even lower mean critical erosion shear stress velocities of 0.62 cm s^{-1} could erode the uppermost fluffy material from mud cores collected in the Baltic Sea.

Strong resuspension events have been reported elsewhere related to internal waves and tidal bores impinging onto the continental shelf and slope, producing bottom and intermediate nepheloid layers originating either at the shelf break or along the continental slope (Van Raaphorst et al., 1998; van Haren, 2009; Walter et al., 2012; Masunaga et al., 2017). A case of BNL and INL formation in deep water by a fall storm was presented by Miles et al. (2013), and for coastal waters by Warner et al. (2008). Bourgault et al. (2014) modeled the potential effects of internal waves impinging on the slope and shelf and presented an acoustic echogram (their Figure 1), clearly distinguishing zones of seafloor resuspension and the formation of BNLs and INLs in the water column along the flank of Ile-aux-Lièvres, an island in the St. Lawrence Estuary, that is morphologically similar to the study area. Jago et al. (1993) noted an increase in resuspension under combined wave/current flows during storms in the southern North Sea similar to our observed data from Hurricane Isaac. They also concluded through model simulations that self-stratification of the boundary layer by resuspended fine sediment may limit further resuspension during storms by reducing bed stress.

Moorings M2, M3, M4, the OC26 ADCP and to a lesser effect moorings M1 and M5 showed the effects of Hurricane Isaac passing over these sites as increased current speeds and strong directional flow on the upper slope. M6 located on the western and weaker side of the hurricane, and moored at 1,267-m depth, recorded easterly to southerly currents during the passage of the hurricane, highlighting the narrow path of energy the hurricane exerted on the seafloor. Highest current speeds were recorded during the days that followed the landfall of the storm with receding storm waters. Elevated current speeds were also seen at the trap station ADCP (**Figure 9**). No significant correlation was found between current speed or direction and material flux when compared over the entire collection time, or individual 18-day periods of the trap schedule, indicating that small-scale events, as seen in the profiling camera data were hidden in the time-averaged flux signal of the sediment trap samples. However, daily mean sediment flux data, collected through the high resolution image interval of the flux camera during the individual large-scale resuspension event of Hurricane Isaac, presented in **Figure 19**, indicate the potential source for a portion of material being located to the east-northeast of the trap location on top or on the flanks of Gloria Dome. This conclusion is very
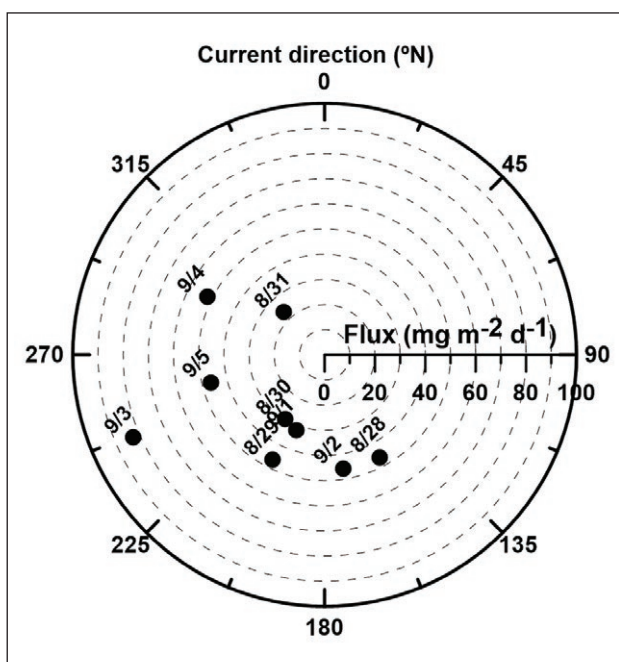

Figure 19: Polar diagram of daily mean particle flux versus daily mean current direction. Polar graph of daily averaged flux calculated from flux camera data as a function of current direction from 28 August 2012 to 5 September 2012. Material during the passage of the storm was mainly moved from east to west with the highest flux on 3 September 2012 after the hurricane had made landfall. DOI: https://doi.org/10.1525/elementa.285.f19

well corroborated by the current flow 18-day time series plotted in **Figure 18**.

During the passage of Hurricane Isaac, δ34S‰ values for both traps at OC26 were within 0.1‰ of each other (cup 4, 21 August 2102; Tables S1 and S2), indicating that the same sources provided the material that was deposited in both traps during this time (**Table 6**). A decrease in mean particle size at the end of August, as measured by the flux camera, indicates a marine "snow storm" of resuspended material induced by the passage of Hurricane Isaac (**Figure 7**). The higher mineral content of aggregates rich in resuspended material would lead to a decrease in size, compared to aggregates formed in the upper ocean (Passow and de la Rocha, 2006; De La Rocha et al., 2008). Although we cannot quantify aggregate concentrations reliably from flux camera photography, a qualitative impression clearly shows a sharp peak in particle concentrations during 1–2 September, also confirming a resuspension event during this period. This resuspension was also captured in traps, with flux in both traps showing the characteristics of resuspended material as defined here (**Table 6**) and their organic matter content differing significantly from all other flux periods (Ziervogel et al., 2016). The vertical extent of this resuspension to >120 mab was also confirmed by the ADCP image, which shows high particle concentrations reaching up to these depths (**Figure 9**). Due to the high energy introduced by this hurricane, resuspension of seafloor

sediments introduced previously sedimented matter into the water column to >120 mab, presumably over a very large area.

Similar occurrences of hurricanes increasing the current field in the deep Gulf of Mexico near the seafloor have been reported. Shay and Elsberry (1987) found evidence that bottom currents in the Desoto Canyon had increased within hours of the initial approach of Hurricane Frederic. Brooks (1983) reported increased current speeds at 700-m depth during the passage of Hurricane Allen in the western Gulf of Mexico. Increased particle flux associated with the passage of hurricanes was reported by Ross et al. (2009), who found that fine material originating from the shelf had increased in their traps deployed at 300-m depth, and Puig et al. (2004) reported an increase in particle flux collected in traps deployed in 120 m of water depth due to storm-induced gravity flows.

Here we did not investigate possible resuspension on larger scales, e.g., caused by deep eddies stemming either directly or indirectly from the Loop current or forming in the Mississippi fan, similar to events described for the North Atlantic (Gardner et al., 2017). Resuspension linked to riverine water flowing in pulses along the continental slope may be another possibility. Such larger scale events may be responsible for the lower lithogenic contribution to flux at 700 m at a site near OC26 (Richey et al., 2014) compared to our deeper flux. Additionally, the composition of glycerol dibiphytanyl glycerol tetraethers (GDGT, membrane lipids used in applications of temperature and pH proxies; Richey and Tierney, 2016) also suggests that subsurface lateral advection of terrestrial material via deep downslope transport regularly contributes to the deep flux at OC26.

Conclusion

Based on our measurements of particle size distribution and settling speed over time compared with sediment trap flux and vertical profiles of particle abundance, we suggest that small-scale resuspension events driven by inertial currents can be imagined as high frequency "noise" on the seasonal curve of flux over time which is dominated by productivity, food webs, mesoscale circulation, riverine input and larger resuspension events. We also suggest that these events may appreciably impact transport and redistribution of lithogenic and organic sedimented material, both locally and in the far field. Especially in regions with varying topography, such events when occurring on a seamount or dome may carry matter farther afield, rather than sediment locally. The frequency and duration of the occurrence of these events is currently unknown; however, based on current meter measurements recorded by the M3 mooring, they could happen as frequently as daily, possibly sustaining a BNL in the form of pulsed material inputs.

Data Accessibility Statements

Data are publicly available through the Gulf of Mexico Research Initiative Information & Data Cooperative (GRIIDC) at https://data.gulfresearchinitiative.org.

Camera data
· https://doi.org/10.7266/N7251G72
· https://doi.org/10.7266/N7QJ7FCD

Sediment Trap and associated ADCP data
· https://doi.org/10.7266/N7PN93PS
· https://doi.org/10.7266/N7JW8BXM
· https://doi.org/10.7266/N7F47M6M
· https://doi.org/10.7266/N79C6VHB
· https://doi.org/10.7266/N737775J

GISR mooring data
· https://doi.org/10.7266/N7F47M38
· https://doi.org/10.7266/N71Z42CN
· https://doi.org/10.7266/N7930R44

Supplemental Files

The supplemental files for this article can be found as follows:

· **Figure S1.** Variance of ESD of particles recorded by the flux camera at OC26. DOI: https://doi.org/10.1525/elementa.285.s1
· **Figure S2.** Flux camera and current meter data during PC3-PC5 at OC26. DOI: https://doi.org/10.1525/elementa.285.s1
· **Figure S3.** Variance of settling speed of particles at OC26. DOI: https://doi.org/10.1525/elementa.285.s1
· **Figure S4.** Zonal and meridional flow at GISR mooring site M4. DOI: https://doi.org/10.1525/elementa.285.s1
· **Figure S5.** Zonal and meridional flow at GISR mooring site M5. DOI: https://doi.org/10.1525/elementa.285.s1
· **Figure S6.** Zonal and meridional flow at GISR mooring site M6. DOI: https://doi.org/10.1525/elementa.285.s1
· **Figure S7.** Bed shear stress at GISR mooring site M4. DOI: https://doi.org/10.1525/elementa.285.s1
· **Figure S8.** Bed shear stress at GISR mooring site M5. DOI: https://doi.org/10.1525/elementa.285.s1
· **Figure S9.** Bed shear stress at GISR mooring site M6. DOI: https://doi.org/10.1525/elementa.285.s1
· **Figure S10.** Block diagram of seafloor around OC26. DOI: https://doi.org/10.1525/elementa.285.s1
· **Table S1.** OC26 flux data measured with the upper sediment trap at 120 mab. DOI: https://doi.org/10.1525/elementa.285.s1
· **Table S2.** OC26 flux data measured with the lower sediment trap at 30 mab. DOI: https://doi.org/10.1525/elementa.285.s1
· **Table S3.** GC600 flux data as measured with the sediment trap at 120 mab. DOI: https://doi.org/10.1525/elementa.285.s1

Acknowledgements

Competing interests
The authors have no competing interests to declare.

Author contributions
- Contributed to conception and design: ARD, VLA, CD, UP, SFD, SLG
- Contributed to acquisition of data: ARD, VLA, CD, SFD, UP, JC
- Contributed to analysis and interpretation of data: CD, ARD, SLG, SFD, JC
- Drafted and/or revised the article: ARD, UP
- Approved the submitted version for publication: ARD, UP, VLA, CD, SFD, JC

References

Alldredge, AL and **Silver, MW** 1988 Characteristics, dynamics and significance of marine snow. *Prog Oceanogr* **20**(1): 41–82. DOI: https://doi.org/10.1016/0079-6611(88)90053-5

Asper, VL 1986 Accelerated Settling of Marine Particulate Matter by 'Marine Snow' Aggregates. DTIC Document. Available at: http://oai.dtic.mil/oai/oai?verb=getRecord&metadataPrefix=html&identifier=ADA166868 Accessed 21 Jun 2016.

Bonnin, J 2004 Short-Term Sediment Resuspension on the Continental Slope and Geochemical Implications: The Faeroe-Shetland Channel. Utrecht, The Netherlands: University Utrecht. Available at: http://dspace/iblrary.uu.nl/handle/1874/587.

Bonnin, J, Koning, E, Epping, E, Brummer, G-J and **Grutters, M** 2005 Geochemical characterization of resuspended sediment on the southeast slope of the Faeroe-Shetland Channel. *Mar Geol* **214**(1–3): 215–233. DOI: https://doi.org/10.1016/j.margeo.2004.10.028

Bonnin, J, Van Haren, H, Hosegood, P and **Brummer, G-JA** 2006 Burst resuspension of seabed material at the foot of the continental slope in the Rockall Channel. *Mar Geol* **226**(3–4): 167–184. DOI: https://doi.org/10.1016/j.margeo.2005.11.006

Bonnin, J, Van Raaphorst, W, Brummer, G-J, van Haren, H and **Malschaert, H** 2002 Intense midslope resuspension of particulate matter in the Faeroe–Shetland Channel: short-term deployment of near-bottom sediment traps. *Deep Sea Res* **49**(8): 1485–1505. DOI: https://doi.org/10.1016/S0967-0637(02)00030-4

Bourgault, D, Morsilli, M, Richards, C, Neumeier, U and **Kelley, DE** 2014 Sediment resuspension and nepheloid layers induced by long internal solitary waves shoaling orthogonally on uniform slopes. *Cont Shelf Res* **72**: 21–33. DOI: https://doi.org/10.1016/j.csr.2013.10.019

Brooks, DA 1983 The wake of Hurricane Allen in the western Gulf of Mexico. *J Phys Oceanogr* **13**(1): 117–129. DOI: https://doi.org/10.1175/1520-0485(1983)013<0117:TWOHAI>2.0.CO;2

Brooks, GR, Larson, RA, Schwing, PT, Romero, I, Moore, C, et al. 2015 Sedimentation pulse in the NE Gulf of Mexico following the 2010 DWH Blowout. *PLOS One* **10**(7): e0132341. DOI: https://doi.org/10.1371/journal.pone.0132341

Chanton, J, Zhao, T, Rosenheim, BE, Joye, S, Bosman, S, et al. 2015 Using natural abundance radiocarbon to trace the flux of petrocarbon to the seafloor following the Deepwater Horizon oil spill. *Environ Sci Technol* **49**(2): 847–854. DOI: https://doi.org/10.1021/es5046524

Chanton, JP, Martens, CS and **Goldhaber, MB** 1987 Biogeochemical cycling in an organic-rich coastal marine basin. 8. A sulfur isotopic budget balanced by differential diffusion across the sediment-water interface. *Geochim Cosmochim Acta* **51**(5): 1201–1208. DOI: https://doi.org/10.1016/0016-7037(87)90212-2

Conti, A, D'Emidio, M, Macelloni, L, Lutken, C, Asper, V, et al. 2016 Morpho-acoustic characterization of natural seepage features near the Macondo Wellhead (ECOGIG site OC26, Gulf of Mexico). *Deep Sea Res Part II* **129**: 53–65. DOI: https://doi.org/10.1016/j.dsr2.2015.11.011

Daly, KL, Passow, U, Chanton, J and **Hollander, D** 2016 Assessing the impacts of oil-associated marine snow formation and sedimentation during and after the Deepwater Horizon oil spill. *Anthropocene* **13**: 18–33. DOI: https://doi.org/10.1016/j.ancene.2016.01.006

Davies, AJ, Duineveld, GCA, van Weering, TCE, Mienis, F, Quattrini, AM, et al. 2010 Short-term environmental variability in cold-water coral habitat at Viosca Knoll, Gulf of Mexico. *Deep Sea Res* **57**(2): 199–212. DOI: https://doi.org/10.1016/j.dsr.2009.10.012

De La Rocha, CL, Nowald, N and **Passow, U** 2008 Interactions between diatom aggregates, minerals, particulate organic carbon, and dissolved organic matter: Further implications for the ballast hypothesis. *Global Biogeochem Cy* **22**(4): GB4005. DOI: https://doi.org/10.1029/2007GB003156

De La Rocha, CL and **Passow, U** 2007 Factors influencing the sinking of POC and the efficiency of the biological carbon pump. *Deep Sea Res Part II* **54**(5–7): 639–658. DOI: https://doi.org/10.1016/j.dsr2.2007.01.004

Diercks, A-R and **Asper, VL** 1997 In situ settling speeds of marine snow aggregates below the mixed layer: Black Sea and Gulf of Mexico. *Deep Sea Res* **44**(3): 385–398. DOI: https://doi.org/10.1016/S0967-0637(96)00104-5

Dike, CH 2015 Marine snow settling velocities at an oil spill site and a control site in the Northern Gulf of Mexico. Hattiesburg, MS, University of Southern Mississippi. Available at: http://aquila.usm.edu/masters_theses/107/ Accessed 26 Jan 2017.

DiMarco, SF, Howard, MK and **Reid, RO** 2000 Seasonal variation of wind-driven diurnal current cycling on the Texas-Louisiana Continental Shelf. *Geophys Res Lett* **27**(7): 1017–1020. DOI: https://doi.org/10.1029/1999GL010491

Emeis, K, Christiansen, C, Edelvang, K, Jähmlich, S, Kozuch, J, et al. 2002 Material transport from the near shore to the basinal environment in the southern Baltic Sea: II: synthesis of data on origin and properties of material. *J Mar Syst* **35**(3): 151–168. DOI: https://doi.org/10.1016/S0924-7963(02)00127-6

Garcia-Pineda, O, MacDonald, I and **Shedd, W** 2014 Analysis of oil-volume fluxes of hydrocarbon-seep formations on the Green Canyon and Mississippi Canyon: A study with 3D-seismic attributes in Combination with satellite and acoustic data. *SPE Reserv Eval Eng* **17**(04): 430–435. DOI: https://doi.org/10.2118/169816-PA

Gardner, WD 1978 Fluxes, dynamics, and chemistry of particulates in the ocean. Woods Hole, Massachusetts, Woods Hole Oceanographic Institution and MIT Available at: http://oai.dtic.mil/oai/oai?verb=getRecord&metadataPrefix=html&identifier=ADA058770 Accessed 21 Jun 2016.

Gardner, WD, Southard, JB and **Hollister, CD** 1985 Sedimentation, resuspension and chemistry of particles in the northwest Atlantic. *Mar Geol* **65**(3): 199–242. DOI: https://doi.org/10.1016/0025-3227(85)90057-X

Gardner, WD, Sullivan, LG and **Thorndike, EM** 1984 Long-term photographic, current, and nephelometer observations of manganese nodule environments in the Pacific. *Earth Planet Sci Lett* **70**(1): 95–109. DOI: https://doi.org/10.1016/0012-821X(84)90212-7

Gardner, WD, Tucholke, BE, Richardson, MJ and **Biscaye, PE** 2017 Benthic storms, nepheloid layers, and linkage with upper ocean dynamics in the western North Atlantic. *Mar Geol* **385**: 304–327. DOI: https://doi.org/10.1016/j.margeo.2016.12.012

Gardner, WD and **Walsh, ID** 1990 Distribution of macroaggregates and fine-grained particles across a continental margin and their potential role in fluxes. *Deep Sea Res* **37**(3): 401–411. DOI: https://doi.org/10.1016/0198-0149(90)90016-O

Giering, SLC, Yan, B, Sweet, J, Asper, V, Diercks, A, et al. 2018 The ecosystem baseline for particle flux in the Northern Gulf of Mexico. *Elem Sci Anth* **6**(1): 6. DOI: https://doi.org/10.1525/elementa.264

Hamm, CE 2002 Interactive aggregation and sedimentation of diatoms and clay-sized lithogenic material. *Limnol Oceanogr* **47**(6): 1790–1795. DOI: https://doi.org/10.4319/lo.2002.47.6.1790

Honjo, S, Doherty, KW, Agrawal, YC and **Asper, VL** 1984 Direct optical assessment of large amorphous aggregates (marine snow) in the deep ocean. *Deep Sea Res* **31**: 67–76. DOI: https://doi.org/10.1016/0198-0149(84)90073-6

Honjo, S, Manganini, SJ and **Cole, JJ** 1982 Sedimentation of biogenic matter in the deep ocean. *Deep Sea Res* **29**(5): 609–625. DOI: https://doi.org/10.1016/0198-0149(82)90079-6

Iversen, MH and **Ploug, H** 2010 Ballast minerals and the sinking carbon flux in the ocean: carbon-specific respiration rates and sinking velocity of marine snow aggregates. *Biogeosciences* **7**(9): 2613–2624. DOI: https://doi.org/10.5194/bg-7-2613-2010

Jago, CF, Bale, AJ, Green, MO, Howarth, MJ, Jones, SE, et al. 1993 Resuspension processes and seston dynamics, southern North Sea. *Philos T Roy Soc A* **343**(1669): 475–491. DOI: https://doi.org/10.1098/rsta.1993.0060

Jaimes, B and **Shay, LK** 2010 Near-inertial wave wake of hurricanes Katrina and Rita over mesoscale oceanic eddies. *J Phys Oceanogr* **40**(6): 1320–1337. DOI: https://doi.org/10.1175/2010JPO4309.1

Joye, SB 2016 The Gulf of Mexico ecosystem – Before, during and after the Deepwater Horizon oil well blowout. *Deep Sea Res Part II* **129**: 1. DOI: https://doi.org/10.1016/j.dsr2.2016.04.022

Joye, SB, Bracco, A, Özgökmen, TM, Chanton, JP, Grosell, M, et al. 2016 The Gulf of Mexico ecosystem, six years after the Macondo oil well blowout. *Deep Sea Res Part II* **129**: 4–19. DOI: https://doi.org/10.1016/j.dsr2.2016.04.018

Kerfoot, WC, Budd, JW, Eadie, BJ, Vanderploeg, HA and **Agy, M** 2004 Winter storms: Sequential sediment traps record *Daphnia* ephippial production, resuspension, and sediment interactions. *Limnol Oceanogr* **49**(4, part 2): 1365–1381. DOI: https://doi.org/10.4319/lo.2004.49.4_part_2.1365

Klaas, C and **Archer, DE** 2002 Association of sinking organic matter with various types of mineral ballast in the deep sea: Implications for the rain ratio. *Global Biogeochem Cyc* **16**(4): 63-1–63-14. DOI: https://doi.org/10.1029/2001GB001765

Klein, H and **Mittelstaedt, E** 1992 Currents and dispersion in the abyssal Northeast Atlantic. Results from the NOAMP field program. *Deep Sea Res* **39**(10): 1727–1745. DOI: https://doi.org/10.1016/0198-0149(92)90026-P

Lampitt, RS 1985 Evidence for the seasonal deposition of detritus to the deep-sea floor and its subsequent resuspension. *Deep Sea Res* **32**(8): 885–897. DOI: https://doi.org/10.1016/0198-0149(85)90034-2

Liu, G, Bracco, A and **Passow, U** 2018 Mesoscale and submesoscale circulation influences sinking particles in the northern Gulf of Mexico. *Elem Sci Anth* (under review).

Maggi, F 2013 The settling velocity of mineral, biomineral, and biological particles and aggregates in water. *J Geophys Res Oceans* **118**(4): 2118–2132. DOI: https://doi.org/10.1002/jgrc.20086

Maggi, F and **Winterwerp, JC** 2004 Method for computing the three-dimensional capacity dimension from two-dimensional projections of fractal aggregates. *Phys Rev E – Stat Nonlinear Soft Matter Phys* **69**: in press. Available at: http://resolver.tudelft.nl/uuid:6078e612-a029-4121-881c-f6d842a2af91 Accessed 11 Dec 2017.

Martens, CS, Mendlovitz, HP, Seim, H, Lapham, L and **D'Emidio, M** 2016 Sustained in situ measurements of dissolved oxygen, methane and water transport processes in the benthic boundary layer at MC118, northern Gulf of Mexico. *Deep Sea Res Part II* **129**: 41–52. DOI: https://doi.org/10.1016/j.dsr2.2015.11.012

Masunaga, E, Arthur, RS, Fringer, OB and **Yamazaki, H** 2017 Sediment resuspension and the generation of intermediate nepheloid layers by shoaling internal bores. *J Mar Syst* **170**: 31–41. DOI: https://doi.org/10.1016/j.jmarsys.2017.01.017

McCave, IN (ed.) 1976 The Benthic Boundary Layer. NATO Science Committee Conference on the Benthic Boundary Layer. New York: Plenum Press. DOI: https://doi.org/10.1007/978-1-4615-8747-7_15

Miles, T, Glenn, SM and **Schofield, O** 2013 Temporal and spatial variability in fall storm induced sediment resuspension on the Mid-Atlantic Bight. *Cont Shelf Res* **63**(Supplement): S36–S49. DOI: https://doi.org/10.1016/j.csr.2012.08.006

Newell, CR, Pilskaln, CH, Robinson, SM and **MacDonald, BA** 2005 The contribution of marine snow to the particle food supply of the benthic suspension feeder, Mytilus edulis. *J Exp Mar Biol Ecol* **321**(2): 109–124. DOI: https://doi.org/10.1016/j.jembe.2005.01.006

Passow, U 2016 Formation of rapidly-sinking, oil-associated marine snow. *Deep Sea Res Part II* **129**: 232–240. DOI: https://doi.org/10.1016/j.dsr2.2014.10.001

Passow, U and **De La Rocha, CL** 2006 Accumulation of mineral ballast on organic aggregates. *Global Biogeochem Cy* **20**(1). DOI: https://doi.org/10.1029/2005GB002579

Passow, U, De La Rocha, CL, Fairfield, C and **Schmidt, K** 2014 Aggregation as a function of and mineral particles. *Limnol Oceanogr* **59**(2): 532–547. DOI: https://doi.org/10.4319/lo.2014.59.2.0532

Passow, U and **Hetland, R** 2016 What happened to all of the oil? *Oceanography* **29**(3): 88–95. DOI: https://doi.org/10.5670/oceanog.2016.73

Passow, U, Ziervogel, K, Asper, V and **Diercks, A** 2012 Marine snow formation in the aftermath of the Deepwater Horizon oil spill in the Gulf of Mexico. *Environ Res Lett* **7**(3): 035301. DOI: https://doi.org/10.1088/1748-9326/7/3/035301

Peine, F, Turnewitsch, R, Mohn, C, Reichelt, T, Springer, B, et al. 2009 The importance of tides for sediment dynamics in the deep sea—Evidence from the particulate-matter tracer [234]Th in deep-sea environments with different tidal forcing. *Deep Sea Res Part I* **56**(7): 1182–1202. DOI: https://doi.org/10.1016/j.dsr.2009.03.009

Pilskaln, CH, Lehmann, C, Paduan, JB and **Silver, MW** 1998 Spatial and temporal dynamics in marine aggregate abundance, sinking rate and flux: Monterey Bay, central California. *Deep Sea Res Part II* **45**(8): 1803–1837. DOI: https://doi.org/10.1016/S0967-0645(98)80018-0

Ploug, H, Terbruggen, A, Kaufmann, A, Wolf-Gladrow, D and **Passow, U** 2010 A novel method to measure particle sinking velocity in vitro, and its comparison to three other in vitro methods. *Limnol Oceanogr Methods* **8**: 386–393. DOI: https://doi.org/10.4319/lom.2010.8.386

Prouty, NG, Fisher, CR, Demopoulos, AWJ and **Druffel, ERM** 2016 Growth rates and ages of deep-sea corals impacted by the Deepwater Horizon oil spill. *Deep Sea Res Part II* **129**: 196–212. DOI: https://doi.org/10.1016/j.dsr2.2014.10.021

Puig, P, Canals, M, Company, JB, Martín, J, Amblas, D, et al. 2012 Ploughing the deep sea floor. *Nature* **489**(7415): 286–289. DOI: https://doi.org/10.1038/nature11410

Puig, P, Madron, XD, de Salat, J, Schroeder, K, Martín, J, et al. 2013 Thick bottom nepheloid layers in the western Mediterranean generated by deep dense shelf water cascading. *Prog Oceanogr* **111**: 1–23. DOI: https://doi.org/10.1016/j.pocean.2012.10.003

Puig, P, Ogston, AS, Mullenbach, BL, Nittrouer, CA, Parsons, JD, et al. 2004 Storm-induced sediment gravity flows at the head of the Eel submarine canyon, northern California margin. *J Geophys Res Oceans* **109**(C3). DOI: https://doi.org/10.1029/2003JC001918

Rees, CE, Jenkins, WJ and **Monster, J** 1978 The sulphur isotopic composition of ocean water sulphate. *Geochim Cosmochim Acta* **42**(4): 377–381. DOI: https://doi.org/10.1016/0016-7037(78)90268-5

Richey, JN, Reynolds, CE, Tappa, E and **Thunell, R** 2014 Weekly resolution particulate flux from a sediment trap in the Northern Gulf of Mexico, 2008–2012. Reston, VA: U. S. Geological Survey. DOI: https://doi.org/10.3133/ofr20141035

Richey, JN and **Tierney, JE** 2016 GDGT and alkenone flux in the northern Gulf of Mexico: Implications for the TEX86 and UK'37 paleothermometers. *Paleoceanography* **31**(12). DOI: https://doi.org/10.1002/2016PA003032

Roberts, HH, Feng, D and **Joye, SB** 2010 Cold-seep carbonates of the middle and lower continental slope, northern Gulf of Mexico. *Deep Sea Res Part II* **57**(21–23): 2040–2054. DOI: https://doi.org/10.1016/j.dsr2.2010.09.003

Roos, P and **Valeur, JR** 2006 A sediment trap and radio-isotope study to determine resuspension of particle reactive substances in the sound between Sweden and Denmark. *Cont Shelf Res* **26**(4): 474–487. DOI: https://doi.org/10.1016/j.csr.2006.01.001

Ross, CB, Gardner, WD, Richardson, MJ and **Asper, VL** 2009 Currents and sediment transport in the Mississippi Canyon and effects of Hurricane Georges. *Cont*

Shelf Res **29**(11–12): 1384–1396. DOI: https://doi.org/10.1016/j.csr.2009.03.002

Shay, LK and **Elsberry, RL** 1987 Near-inertial ocean current response to Hurricane Frederic. *J Phys Oceanogr* **17**(8): 1249–1269. DOI: https://doi.org/10.1175/1520-0485(1987)017<1249:NIOCRT>2.0.CO;2

Shipe, RF and **Brzezinski, MA** 2001 A time series study of silica production and flux in an eastern boundary region: Santa Barbara Basin, California. *Global Biogeochem Cy* **15**(2): 517–531. DOI: https://doi.org/10.1029/2000GB001297

Shipe, RF and **Brzezinski, MA** 2003 Siliceous plankton dominate primary and new productivity during the onset of El Niño conditions in the Santa Barbara Basin, California. *J Mar Syst* **42**(3): 127–143. DOI: https://doi.org/10.1016/S0924-7963(03)00071-X

Spencer, LJ, DiMarco, SF, Wang, Z, Kuehl, JJ and **Brooks, DA** 2016 Asymmetric oceanic response to a hurricane: Deep water observations during Hurricane Isaac. *J Geophys Res Oceans* **121**(10): 7619–7649. DOI: https://doi.org/10.1002/2015JC011560

Sutyrin, GG, Rowe, GD, Rothstein, LM and **Ginis, I** 2003 Baroclinic eddy interactions with continental slopes and shelves. *J Phys Oceanogr* **33**(1): 283–291. DOI: https://doi.org/10.1175/1520-0485(2003)033<0283:BEIWCS>2.0.CO;2

Tamelander, T, Spilling, K and **Winder, M** 2017 Organic matter export to the seafloor in the Baltic Sea: Drivers of change and future projections. *Ambio* **46**(8): 842–851. DOI: https://doi.org/10.1007/s13280-017-0930-x

Tesi, T, Langone, L, Ravaioli, M, Giglio, F and **Capotondi, L** 2012 Particulate export and lateral advection in the Antarctic Polar Front (Southern Pacific Ocean): One-year mooring deployment. *J Mar Syst* **105**–**108**: 70–81. DOI: https://doi.org/10.1016/j.jmarsys.2012.06.002

Turnewitsch, R, Falahat, S, Nycander, J, Dale, A, Scott, RB, et al. 2013 Deep-sea fluid and sediment dynamics—Influence of hill- to seamount-scale seafloor topography. *Earth-Sci Rev* **127**: 203–241. DOI: https://doi.org/10.1016/j.earscirev.2013.10.005

Valentine, DL, Fisher, GB, Bagby, SC, Nelson, RK, Reddy, CM, et al. 2014 Fallout plume of submerged oil from *Deepwater Horizon*. *Proc Natl Acad Sci* **111**(45): 15906–15911. DOI: https://doi.org/10.1073/pnas.1414873111

Valipour, R, Boegman, L, Bouffard, D and **Rao, YR** 2017 Sediment resuspension mechanisms and their contributions to high-turbidity events in a large lake. *Limnol Oceanogr* **62**(3): 1045–1065. DOI: https://doi.org/10.1002/lno.10485

van Haren, H 2009 Using high sampling-rate ADCP for observing vigorous processes above sloping [deep] ocean bottoms. *J Mar Syst* **77**(4): 418–427. DOI: https://doi.org/10.1016/j.jmarsys.2008.10.012

Van Raaphorst, W, Malschaert, H and **Van Haren, H** 1998 Tidal resuspension and deposition of particulate matter in the Oyster Grounds, North Sea. *J Mar Res* **56**(1): 257–291. DOI: https://doi.org/10.1357/002224098321836181

Walsh, I, Fischer, K, Murray, D and **Dymond, J** 1988 Evidence for resuspension of rebound particles from near-bottom sediment traps. *Deep Sea Res* **35**(1): 59–70. DOI: https://doi.org/10.1016/0198-0149(88)90057-X

Walter, RK, Woodson, CB, Arthur, RS, Fringer, OB and **Monismith, SG** 2012 Nearshore internal bores and turbulent mixing in southern Monterey Bay. *J Geophys Res Oceans* **117**(C7): 017. DOI: https://doi.org/10.1029/2012JC008115

Warner, JC, Butman, B and **Dalyander, PS** 2008 Storm-driven sediment transport in Massachusetts Bay. *Cont Shelf Res* **28**(2): 257–282. DOI: https://doi.org/10.1016/j.csr.2007.08.008

Wilson, AM 2016 Lateral transport of suspended particulate matter in nepheloid layers along the Irish continental margin-a case study of the Whittard Canyon, North-East Atlantic Ocean. National University of Ireland, Galway, Earth and Ocean Sciences. Available at: https://aran.library.nuigalway.ie/handle/10379/6047.

Yan, B, Passow, U, Chanton, JP, Nöthig, E-M, Asper, V, et al. 2016 Sustained deposition of contaminants from the Deepwater Horizon spill. *Proc Natl Acad Sci* **113**(24): E3332–E3340. DOI: https://doi.org/10.1073/pnas.1513156113

Yuan, D 2002 A numerical study of barotropically forced intrusion in DeSoto Canyon. *J Geophys Res Oceans* **107**(C2): 2-1–2-15. DOI: https://doi.org/10.1029/2001JC000793

Zhang, H, Khatibi, M, Zheng, Y, Lee, K, Li, Z and **Mullin, JV** 2010 Investigation of OMA formation and the effect of minerals. *Mar Pollut Bull* **60**(9): 1433–1441. DOI: https://doi.org/10.1016/j.marpolbul.2010.05.014

Zhang, X, DiMarco, SF, Smith, DC, Howard, MK, Jochens, AE, et al. 2009 Near-resonant ocean response to sea breeze on a stratified continental shelf. *J Phys Oceanogr* **39**(9): 2137–2155. DOI: https://doi.org/10.1175/2009JPO4054.1

Ziervogel, K and **Bohling, B** 2003 Sedimentological parameters and erosion behaviour of submarine coastal sediments in the south-western Baltic Sea. *Geo-Mar Lett* **23**(1): 43–52. DOI: https://doi.org/10.1007/s00367-003-0123-4

Ziervogel, K, Dike, C, Asper, V, Montoya, J, Battles, J, et al. 2016 Enhanced particle fluxes and heterotrophic bacterial activities in Gulf of Mexico bottom waters following storm-induced sediment resuspension. *Deep Sea Res Part II* **129**: 77–88. DOI: https://doi.org/10.1016/j.dsr2.2015.06.017